



ORIGINAL RESEARCH ARTICLE

# Effect of Process Conditions on Mechanical and Metallurgical Properties of Wire Arc Additively Manufactured 316L Stainless Steel

Gaurav Kishor , Krishna Kishore Mugada, Raju Prasad Mahto, and Vishvesh Badheka

Submitted: 17 October 2023 / Revised: 11 May 2024 / Accepted: 27 May 2024

Understanding the microstructural formation in the wire arc additive manufacturing (WAAM) process is highly important, and it is very challenging to predict the microstructure formation and mechanical properties of the as-deposited samples. The present study investigates the effect of process conditions such as current, travel speed, and gas flow rate on the mechanical and metallurgical properties of SS 316L stainless steel. The microstructure of the as-deposited samples reveals a diffusion zone with columnar dendrites and equiaxed grains in the bottom layers, skeletal  $\delta$ -ferrite in the middle layers, and coarse dendritic structure in the top layers, respectively. Microstructure development in the samples' vertical direction shows pearlitic-ferritic grains to bainitic lamellae. The maximum and minimum grain sizes at the fusion region are  $18 \pm 1 \mu\text{m}$  and  $7.56 \pm 1 \mu\text{m}$ . Further, the using design of experiments technique the parameters are optimized for maximum tensile strength and hardness. The results show that travel speed has the highest impact on tensile strength (688 MPa), followed by current and gas flow rate. The main process parameter that affects the hardness (198 HV) is current followed by wire feed rate and gas flow rate. A relation of the strength concerning strain and temperature for various conditions is established using the Johnson–Cook model. The formation of  $\gamma$ -Fe, austenite, MnSi, Fe-Ni, etc., are observed in the x-ray diffraction images of as-deposited samples. The dislocation density varies from  $1.745 \times 10^{-4}$  to  $9.922 \times 10^{-4} \text{ nm}^{-2}$ , and the microstrain is varying from  $2.43 \times 10^{-3}$  to  $3.8 \times 10^{-3}$ . The fracture surfaces of as-deposited samples show the formation of dimples and river facets.

**Keywords** dislocation density, fracture surface, grain size, microstructure, wire arc additive manufacturing, XRD

## 1. Introduction

Since several decades, several manufacturing process, and several advancements have occurred to manufacture complex parts and objects with optimum time and cost. One such significant advancement is additive manufacturing in which the layer-by-layer deposition occurs the manufacture complex

This invited article is part of a special topical issue of the *Journal of Materials Engineering and Performance* on Advanced Materials Manufacturing. The issue was organized by Antonello Astarita, University of Naples Federico II; Glenn S. Daehn, The Ohio State University; Emily Kinsler, ARPA-E; Govindarajan Muralidharan, Oak Ridge National Laboratory; John Shingledecker, Electric Power Research Institute, Le Zhou, Marquette University, and William Frazier, Pilgrim Consulting, LLC, and Editor, *JMEP*; on behalf of the ASM International Advanced Manufacturing Technical Committee.

**Gaurav Kishor**, **Krishna Kishore Mugada**, and **Raju Prasad Mahto**, Department of Mechanical Engineering, Sardar Vallabhbhai National Institute of Technology Surat, Surat 395007, India; and **Vishvesh Badheka**, Department of Mechanical Engineering, Pandit Deendayal Energy University, Raisan, Gandhinagar 382007, India. Contact e-mail: mugada.krishnakishore@gmail.com.

components as compared to conventional processes (Ref 1). The three forms of energy sources for additive manufacturing for metals are laser, electron beam, and electric arc (Ref 2). The wire arc additive manufacturing (WAAM) uses an electric arc as a heat source to melt the wire feed stock and deposit it layer-by-layer to produce the 3D components with the precise movement of a welding torch (Ref 3). Researchers use different types of arc sources such as GMAW (gas metal arc welding), PAW (plasma arc welding), GTAW (gas tungsten arc welding), etc., to produce the components using the WAAM process (Ref 1-3). Over the past few years, WAAM has gained acceptance and is gradually replacing its rival technologies for producing large, intricate metallic components. Its outstanding benefits include minimal setup and human involvement, quick production due to high deposition rates, minimal material removal, and lower material costs for wire compared to other additive manufacturing processes such as power-based processes (Ref 3, 4). On the other hand, induced residual stresses and distortions, as well as poor workpiece surface conditions brought on by the waviness and humping defect, limit the WAAM process to manufacture components for critical applications, because of poor surface finish secondary operations like finishing are required for WAAM-produced components (Ref 5).

Due to stainless steel's excellent qualities of superior corrosion resistance, good weld-ability, high strength and ductility, and relatively low cost, it is used in a variety of industrial applications, including marine and offshore applications, automobiles, petrochemical facilities, and nuclear

reactors. Molybdenum (around 2-3%) content in the stainless steel increases the resistance to pitting and corrosion. 316L stainless steel is a chromium-nickel-molybdenum alloy that has a very low carbon content (approximately 0.03%) and a low susceptibility to carbide precipitation (Ref 6).

Saboori et al. (Ref 7) discussed in detail the various challenges associated with the deposition of stainless steels in both the direct energy deposition (DED) process and the wire arc additive manufacturing process. The observations reveal the nonuniform microstructure from bottom to top of the as-deposited specimens in WAAM compared to the DED process. Further, Liberini et al. (Ref 8) investigated ER70S-6 steels and observed that the as-deposited wall structure was divided into three zones- the lower zone, which was dominated by pearlite bands, the middle zone, which was dominated by ferrite equiaxed grains, and the top zone is dominated by bainite. Mai et al. (Ref 9) worked on the 308L steels and observed the mechanical properties of as-deposited samples have 40-54% strength compared with the wrought 308L steels. Kumar et al. (Ref 10) studied the effect of process parameters on the local temperature cycle which is responsible for solidification behavior. Ferrite with pearlite structures can be seen close to the base of the manufactured portion. Surface flaws like cracks and porosity are most frequently observed at the interface. The flat and circular walls' respective microhardness values are 162.80 and 172.19 HV. Youheng et al. (Ref 11) further studied the bead geometry of the as-deposited samples of bainite steel, and the results show that the surface roughness of the WAAM samples is high compared with the laser-based additively manufactured samples. Kumar and Maji (Ref 12) discovered that the multi-beads produced by WAAM have a microstructure full of many dendritic grains. The produced multi-bead wall yield strength and ultimate tensile strength were 336, and 544 MPa, respectively, and the average Vickers microhardness is 187 HV. Waqas et al. (Ref 13) worked on the parameter optimization for the effective area of the WAAM-deposited specimen. They identified that travel speed has a maximum impact on bead height followed by other parameters like voltage and current. Venkatarao et al. (Ref 14) summarized that wire feed rate and welding speed have an impact on the width and height of the weld bead, whereas current and torch angles mostly affect the depth of the weld bead. Wire feed speed (WFS) was observed to improve the multilayer structure's surface quality as reported by Xiong et al. (Ref 15). This is further investigated by Yuan et al. (Ref 16) who identified that along with wire feed rate, the travel speed is also important for improving the deposition rate.

Overall, it is observed that there are significant studies on austenitic stainless steels deposited by the WAAM process however understanding the microstructural development at different zones of the as-deposited samples for various process conditions such as current, travel speed, and gas flow rate is very limited, also the establishment of the Johnson-Cook (J-C) model to understand the behavior of the material under various strain conditions are scarce. Therefore, in the present investigation, the effect of process conditions on the grain size, microstructure at the interface zone, bottom layers, middle layers, and top layers of as-deposited specimens is studied. Further, the tensile strength, hardness, analysis of the phases, dislocation density, and fracture surfaces are investigated for the 316L stainless steel.

## 2. Materials and Methods

### 2.1 Heat source and materials

The gas metal arc welding (GMAW) equipment of model MIG-530 and make KEMPPI PRO system is used for the deposition of 316L stainless steel (here onward referred as SS 316L). The experimental setup for the current work is depicted in Fig. 1(a). The computer interface was utilized in the current experimental configuration to program CNC code and provides input to the controller. The deposition torch can be moved along the three axes of  $x$ ,  $y$ , and  $z$  direction controlled with a CNC controller through CNC code. Before the program began, shielding gas was given through the setup to protect the deposit.

A commercial filler wire with a diameter of 1.2 mm and a substrate of the same material as SS 316L is used. The chemical composition of the filler wire and substrate is given in Table 1.

Figure 1(b) shows tensile and hardness sample locations that are extracted from the as-deposited SS 316L specimen. Figure 1(d) shows four locations of the microstructure specimens and Fig. 1(f) shows the dimensions (mm) of tensile specimens according to ASTM E8 standard.

The etchant used to reveal the microstructure of the samples was (HCl: HNO<sub>3</sub>=3:1) for 15 s etching time. For tensile testing, 1.2 mm/min crosshead speed is used. A strip of full height is taken from bottom to top as shown in Fig. 1(b) the load is 10 kgf and dwell time is taken 10 s for hardness measurement.

### 2.2 Design of Experiments

The study is focused on examining the effects of input parameters such as current, travel speed, and gas flow rate on the mechanical properties of as-deposited layers. Based on the pilot experiments and by visual inspection of the as-deposited specimens, the range of various process parameters is fixed. The current varies from 100-40 A, and below 100 A it is observed that the melting rate of SS 316L is poor, and above 140A it is observed that the waviness in the first few layers is damaging the dimensional accuracy (Ref 9, 11). Similarly, for the travel speed, the values are restricted in the range of 200-280 mm/min, and for the gas flow rate, the range is 10-20 L/min. Altering the travel speed below 200 mm/min increases the bead height and at higher traverse speed the bead width is higher.

Therefore, for an optimum bead geometry, the range is limited to 200-280 mm/min. If the travel speed is higher, then it leads to insufficient weld penetration. Insufficient penetration means that the weld does not fully fuse with the base metal, resulting in a weak and shallow weld joint. This lack of fusion can compromise the weld's strength and integrity (Ref 3).

Further, the lower gas flow rates below 10 L/min allow the heat to be absorbed by the inner layers of the as-deposited samples leading to coarse dendritic structures, and increasing the gas flow rate beyond 20 L/min creates porosity formation in the inner layers. Gas flow rate also helps to maintain a stable and smooth arc during deposition which is essential for achieving a consistent weld bead and reducing the likelihood of arc interruptions or "arc blow." Excessive spatter can be problematic during GMAW, as it creates additional clean-up and can lead to weld defects. Proper gas flow helps in reducing spatter by providing a stable environment for the welding process. At higher transverse speed and higher shielding gas flow rate, large number of process-related pores takes place due

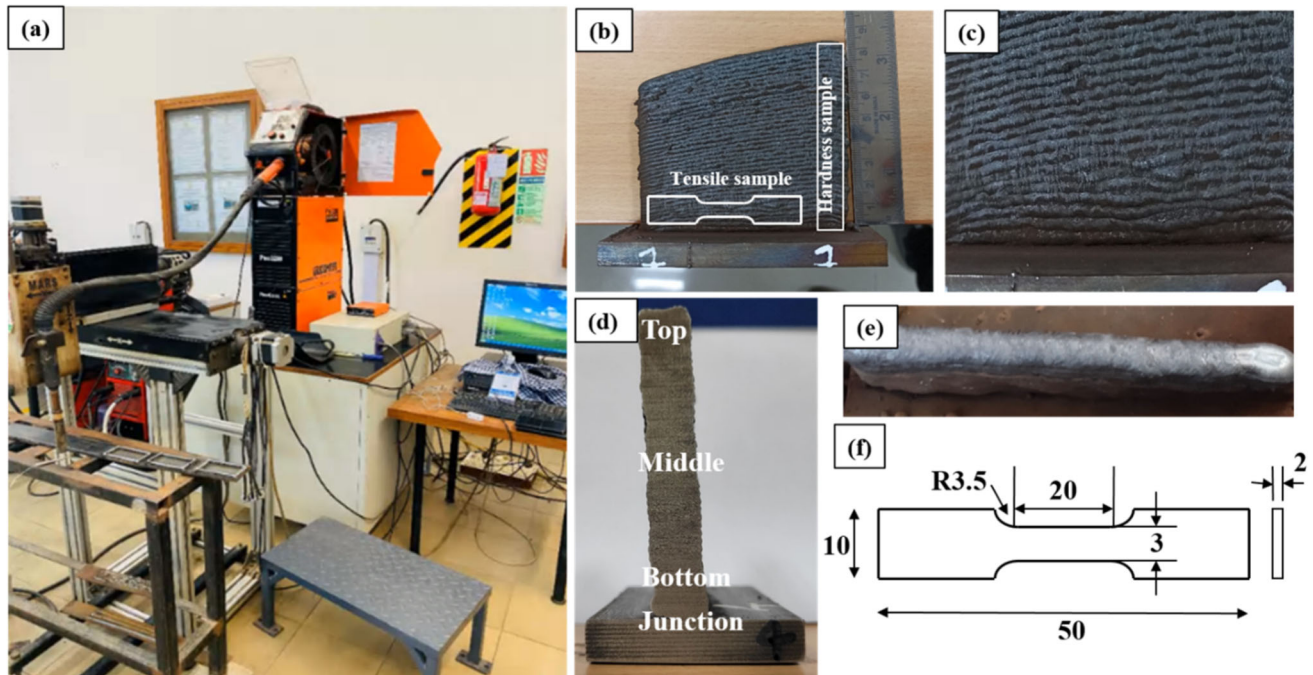


**Fig. 1** (a) GMAW-based WAAM experimental setup, (b) tensile and hardness specimens' extracted from as-deposited samples (c) bead appearance, (d) location of microstructure samples, (e) top view of the wall, and (f) tensile specimen dimensions (mm)

**Table 1** Chemical compositions of the SS 316L wire and substrate (wt.%)

Elements	C	Cr	Ni	Mo	Mn	Si	S	P	Fe
wt.%	0.013	19.24	12.92	2.64	1.68	0.30	0.0021	0.020	Bal.

**Table 2** Factors and levels of the input parameters

Levels	Current, A	Travel speed, mm/min	Gas flow rate, L/min
-1	100	200	10
0	120	240	15
+1	140	280	20

to higher turbulent mixing (Ref 3). Therefore, the range of process conditions selected for investigation in the present study is shown in Table 2. The process parameters that are constant during the entire deposition process are shown in Table 3. Taguchi's L9 orthogonal array is used to reduce the number of experiments and optimize the process parameters with 9 experiments as shown in Table 4. Analysis of variance (ANOVA) is performed to understand the percentage contribution of each process parameter.

### 3. Results and Discussion

#### 3.1 Microstructures of As-Deposited Thin-Walled SS 316L Samples

From the deposited wall, four samples were extracted from different locations the top region, middle region, bottom region,

**Table 3** Constant process parameters and their values

Sr. No.	Parameters	Value
1.	Welding mode	MIG-pulse mode
2.	Voltage	20 V
3.	Wire feed rate	3.2 m/min
4.	Arc length	20 mm
5.	Total number of layers	40
6.	Dwell time	30 s
7.	Shielding gas	Pure argon
8.	Filler wire diameter	1.2 mm

and junction region which is composed of the base plate and initially deposited layer can be shown in Fig. 1(d).

Figure 2 shows with the increase of the current from 100 to 140 A, the size of the columnar dendrites grows with the increased skeletal  $\delta$ -ferrite sites. At the current of 140 A and travel speed of 200 m/min, it is noticed that the solidified liquid molten forms a dendrite with larger arm spacing with a lower hardness of 175 HV. As the current is increasing the heat input is increased increasing the dendrite size which reduces the hardness from 183 to 175 HV. Similarly, at a constant travel speed of 240 mm/min, and varying the current the grain size is becoming coarser and the regions of lathy  $\delta$ -ferrite sites are reducing, thus showing less resistance to the external load as

**Table 4** L<sub>9</sub> orthogonal array layout with process parameters

Experiment No.	Current, A	Travel speed, mm/min	Gas flow rate, L/min
S1	100	200	10
S2	100	240	15
S3	100	280	20
S4	120	200	15
S5	120	240	20
S6	120	280	10
S7	140	200	20
S8	140	240	10
S9	140	280	15

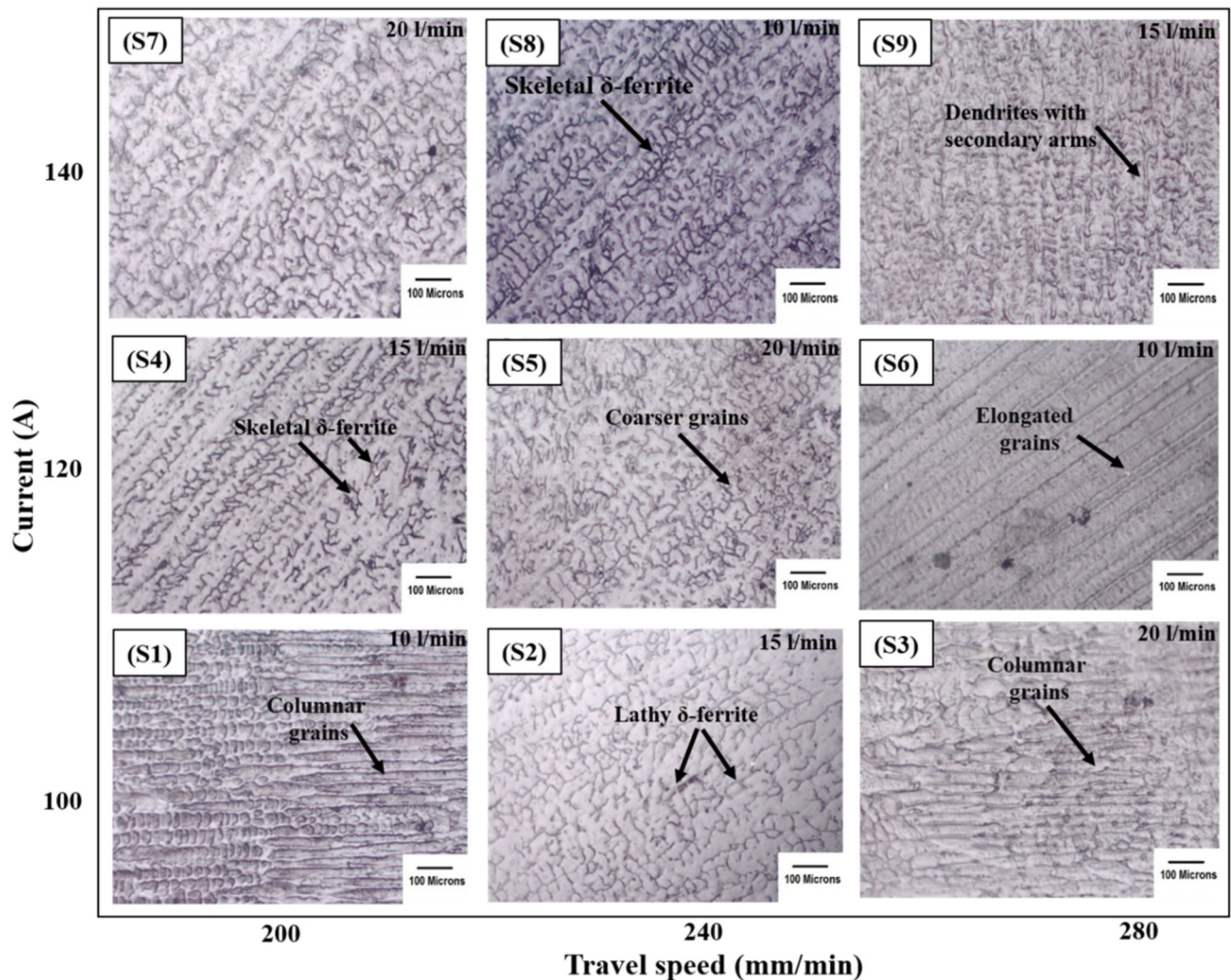


**Fig. 2** Microstructure of as-deposited specimens at the top region for various conditions

observed by the hardness measurements. The hardness values varied from 192 HV at 100 A to 178 HV at 140 A.

However, by increasing the current and travel speed simultaneously, an optimum condition of 120 A, 280 mm/min, and 10 L/min is obtained with a hardness of 190 HV. At lower gas flow rates of 10 L/min and higher travel speeds of 280 mm/min, the dendrite arm spacing is less compared with the higher gas flow rates (20 L/min) which results in higher hardness (190 HV).

The conditions S5, and S7 at 20 L/min show a low hardness value of range 170-183 HV due to the formation of the coarse columnar grains with larger arm spacing. (S\* in the microstructure indicates the sample number as shown in the Table 4.) Similarly, the conditions S4, S2, and S9 at a gas flow rate of 10 L/min show a typical hardness of 175-192 HV due to the large skeletal and lathy  $\delta$ -ferrite grain boundaries. The conditions S1, S6, and S8 show hardness in the range of 178 HV to 190 HV at a gas flow rate of 15 L/min and resulted in the maximum

hardness due to the formation of the columnar grains, and they are enlarged during the solidification with increased travel speed.

As shown in Fig. 3, with increased current conditions from 100 to 140 A in the middle layer, the coarse dendrites are forming which reduces the hardness from 184 to 177 HV. A similar behavior is observed for the higher travel speed conditions for 240 and 280 mm/min. Further by increasing the current and travel speed simultaneously, an optimum condition of 100 A, 280 mm/min travel speed, and 20 L/min gas flow rate is obtained with a hardness of 188 HV. At lower gas flow rates of 10 L/min and higher travel speeds of 280 mm/min, the dendrite arm spacing is reducing.

The conditions S3, S5, and S7 at 20 L/min show a low hardness value of range 177-188 HV due to the formation of the coarse columnar grains with larger arm spacing. Similarly, the conditions S2, S4, and S9 at a gas flow rate of 10 L/min show a typical hardness of 172-182 HV due to the large skeletal and lathy  $\delta$ -ferrite grain boundaries (Ref 9). The conditions S1, S6, and S8 show hardness in the range of 173-184 HV at a gas flow rate of 15 L/min and resulted in the maximum hardness due to the formation of the columnar grains and they are enlarged during the solidification with increased travel speed.

At the bottom portion of the samples with increasing current and keeping travel speed constant size of the grains increased as shown in Fig. 4. At high current and low travel speed, dendritic structure is almost invisible and lathy  $\delta$ -ferrite in some amount takes place with coarse grains as seen in Fig. 4. Condition S3 which has a minimum current value and maximum travel speed gives a maximum hardness value of 201 HV at the same time condition S7 which has a maximum current value and minimum travel speed is the worst condition for hardness. At a minimum gas flow rate of 10 L/min and maximum travel speed condition S6 shows equiaxed formation of grains.

If microstructure is compared concerning distance from the base plate tends to change from columnar grains to equiaxed grains as moves away from the substrate and toward the middle zone. Equiaxed grains develop in all directions and are generally spherical (Ref 9). Dendritic development in the intermediate zone is often less apparent than it is in the near-substrate area. This is due to the cooling rates being a little slower, which allows for a finer grain structure (Ref 10).

The junction zone between the base plate and the initial layer of the weld bead is defined as the diffusion zone at this line melting of the base plate and filler wire takes place there is no heat-affected zone at this line. As shown in Fig. 5 at a

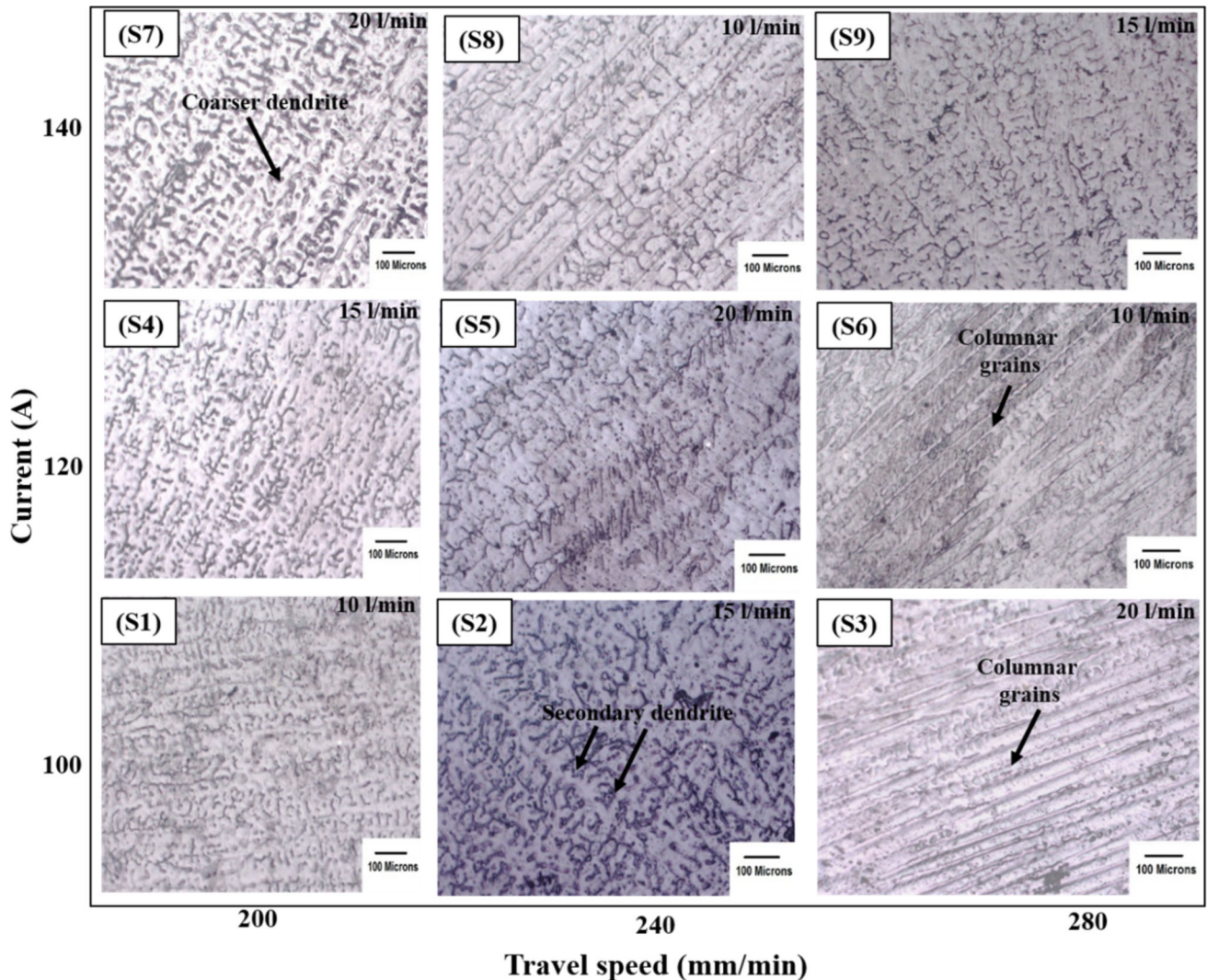
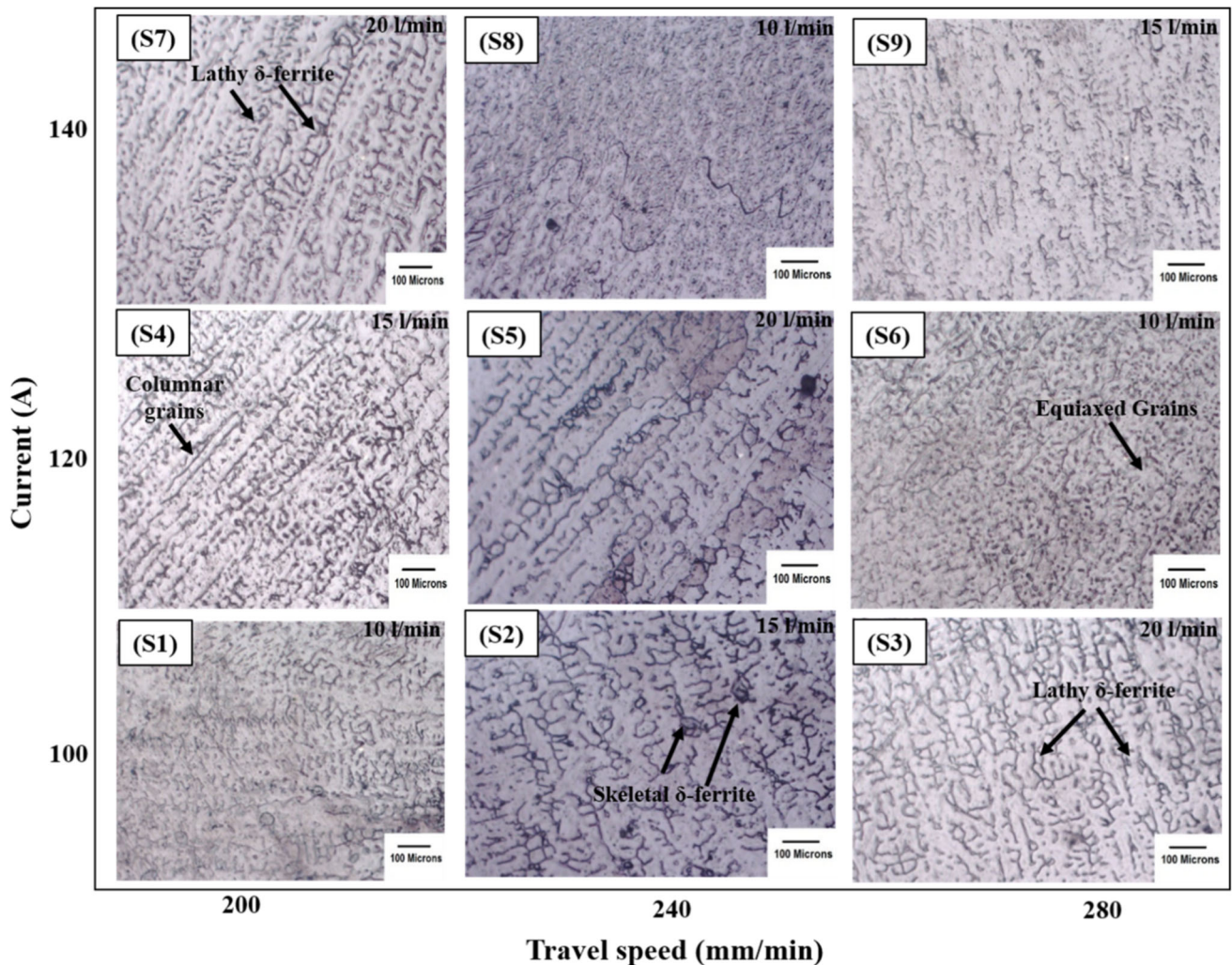


Fig. 3 Microstructure of as-deposited specimens at the middle region for various conditions



**Fig. 4** Microstructure of as-deposited specimens at the bottom region for various conditions

constant travel speed of 200 mm/min with increasing current value fusion zone thickness decreases. At the current value 140 A and minimum travel speed value 200 mm/min diffusion zone is not visible because due to high heat input complete melting of the base plate takes place.

In the near-substrate region, the microstructure is typically characterized by dendritic growth. This is a result of the rapid solidification of the molten metal as it comes in contact with the relatively cool substrate (Ref 18). Dendrites are tree-like crystal structures that form during solidification. As the material solidifies, columnar grains form perpendicular to the substrate takes place as depicted in conditions S2, S5, and S6. These columnar grains grow from the substrate upwards as shown in Fig. 5. The orientation of these grains is influenced by the temperature gradient and solidification rate (Ref 21).

As compared to the upper layers, the grain size in the near-substrate region may be coarser. This is because the rapid solidification leads to smaller, finer grains in the upper layers. There is a heat-affected zone close to the material that has been deposited. High temperatures are present here, yet the area does not completely melt. Phase changes and partial recrystallization traits will be visible in the HAZ microstructure. As a result of the WAAM process' quick cooling, martensite may develop in some places.

Rapid cooling conditions are favorable for the production of Steel's metastable phase which is called martensite. It could see Widmanstätten ferrite develop, depending on the cooling rate and alloy composition. This particular ferrite type only forms in particular orientations to the austenite matrix (Ref 9). Further, the sizes of the grain structure with aspect ratio for various as-deposited samples are estimated and discussed in detail in Sect. 3.2.

### 3.2 Grain Structure

The formation of grains at the junction of the first layer and the substrate plate where diffusion occurs is shown schematically in Fig. 6. Near the interface region due to the conduction of the heat from the deposited layers, the solidification of the molten metal is rapid and results in the fine-grained structure near the diffusion zone. When a liquid substance solidifies, a crystal growth mechanism known as dendritic growth takes place. Dendrites, branching, and tree-like structures are what are produced as a result (Ref 5).

An outline of the dendritic growth process involves small crystals known as nuclei are formed at the beginning of the process. These nuclei develop in various parts of the liquid metal at random. Impurities, foreign particles, or even existing crystals can cause nucleation (Ref 6). A nucleus serves as a

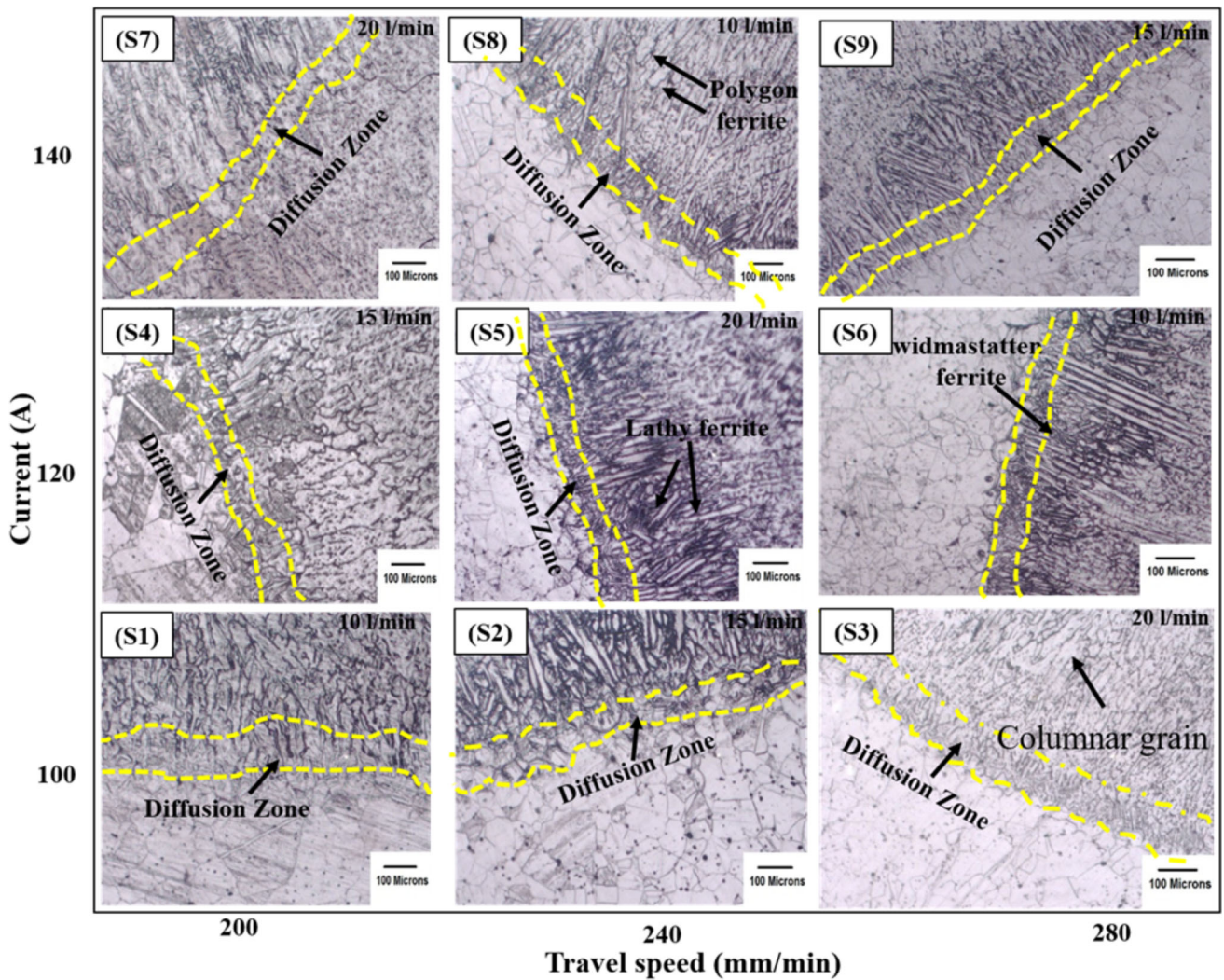


Fig. 5 Microstructure of as-deposited specimens at the junction of base plate and initial layers' of bead for various conditions

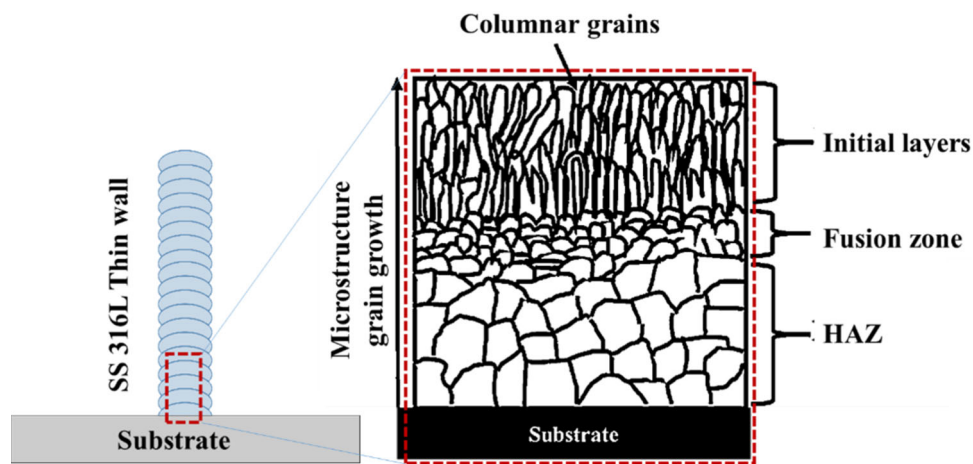


Fig. 6 Schematic representation of grain formation from the substrate in the WAAM process

seed (primary) crystal after it has formed. Atoms from the nearby liquid are drawn to the seed crystal's solid surface, where they join the already-existing lattice structure. As a result, a crystal structure develops. The direction of crystal

formation is not constant. As opposed to that, it happens more frequently along specific crystallographic orientations. This indicates that the dendritic branches develop in particular directions (Ref 7). The final structure has numerous branches,

like a tree. The secondary and tertiary branches are both smaller and more numerous, although the primary dendritic arms are bigger as shown in Fig. 6. Due to the accumulation of heat from the previously deposited layers, the size of the grains is coarser compared to the initial layers where heat is transferred to the substrate by conduction (Ref 8).

Grain size is measured by ImageJ bundled with 64-bit Java 8 software for all conditions at three different conditions heat-affected zone, fusion zone, and initial layer. The grain size of the fusion zone for all samples is represented in Fig. 7. Among all samples condition S4 has the maximum grain size at the fusion region of 18  $\mu\text{m}$  and condition S6 has a minimum grain size of 8  $\mu\text{m}$ .

Several crucial process variables in wire arc additive manufacturing (WAAM) affect the formation of grains in the deposition of material. These factors have an impact on the material's thermal history, which in turn affects grain size and orientation. In this work, three parameters vary for different conditions current, torch travel speed and gas flow rate for conditions S4 and S6 current value is the same but

the travel speed varies from 200 to 280 mm/min, respectively.

For variation in grain size, travel speed is a key factor that directly affects the thermal history of the deposited material and, as a result, the formation of grains. Due to continued exposure of the heat from the arc, slower travel speed might result in a greater heat-affected zone (HAZ). This may have an impact on the thermal history and, as a result, the grain structure. Faster travel speeds cause solidification to occur more quickly, which can encourage finer grain formations, affecting the tensile properties as discussed in Sect. 4. Slower travel speeds, on the other hand, give the substance more time to solidify and may lead to larger grains (Ref 18).

The aspect ratio can provide information about the grains' crystallographic orientation. While elongated grains indicate a preferred orientation, equidimensional (roughly equal length and breadth) grains show isotropic crystallographic orientations (Ref 7). Equidimensional grains can develop in igneous rocks by fast cooling, but elongated grains can arise through processes such as metamorphism. While longer grains could be stronger along their long axes, they are more likely to break

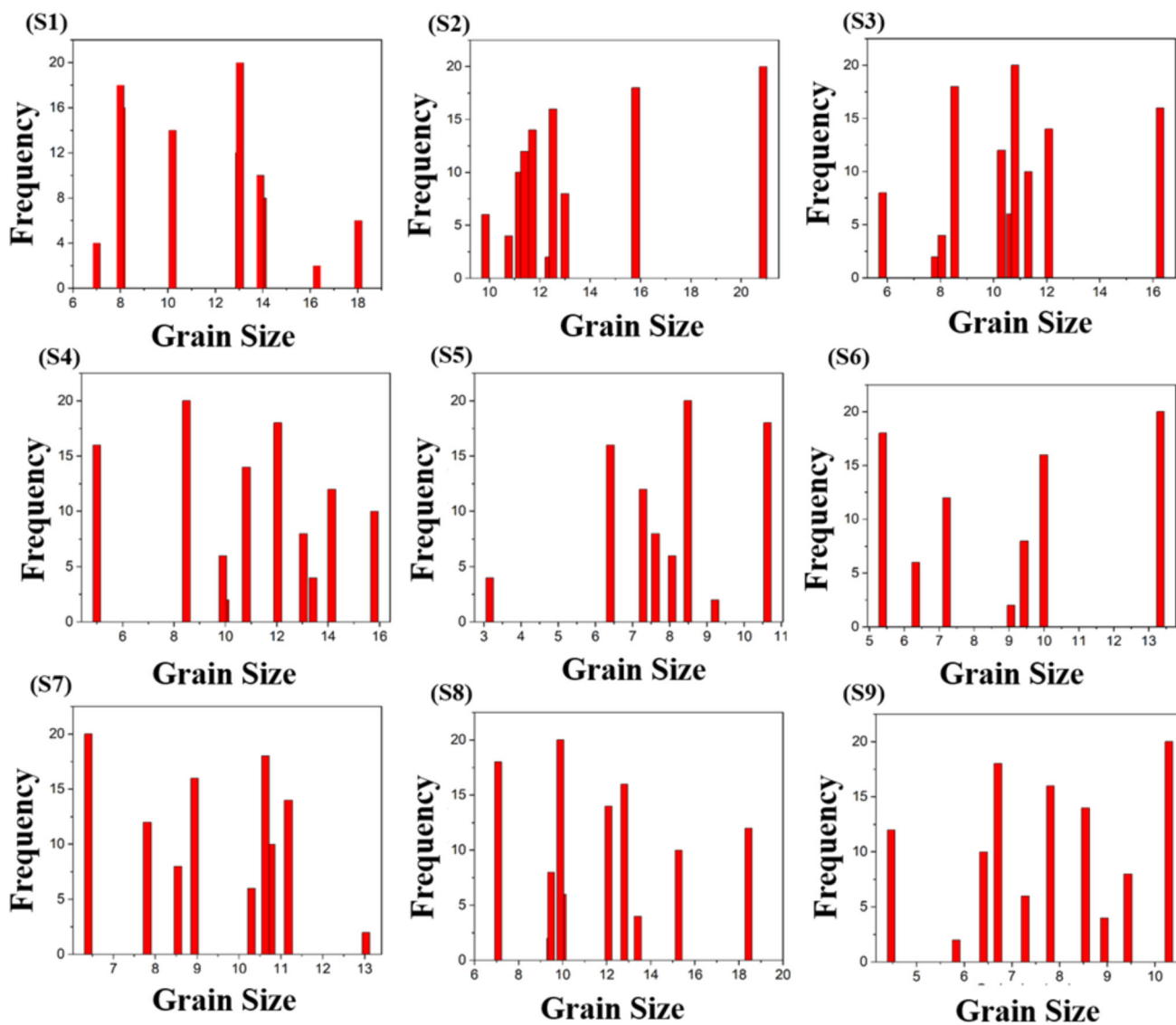


Fig. 7 Grain size for all conditions at fusion region



along their short axes (Ref 21). Aspect ratios can affect a material's permeability (the ease with which fluids can pass through it) and porosity (the amount of empty spaces inside the material). Anisotropic permeability may result from very elongated grains (Ref 22).

The aspect ratio is calculated for the same samples by dividing the largest and smallest dimensions (Ref 17). For all conditions aspect ratio, Fig. 8 is calculated for three regions heat-affected zone, the fusion zone, and the initial layer. The grains of various sizes and aspect ratios mentioned in Fig. 7 and 8 are further used to correlate the tensile and hardness properties as discussed in Sects. 4 And 5, respectively.

### 3.3 XRD Analysis

Figure 9 shows the phase composition analysis of the deposited samples for different conditions at the bottom region. The major phases are observed to be austenite, Fe-Ni, and  $\gamma$ -Fe. According to the phase diagram in condition S2, highest peak occurred at angle  $50^\circ$  with the composition of iron-nickel and iron silicide carbide with d-spacing 2.07923 [Å] and 0.94355 [Å], respectively. In all conditions, the highest peak takes place at approximately  $50^\circ$  angles and the composition has a maximum percentage of austenite and  $\gamma$ -Fe. The equilibrium microstructure of SS 316L is a completely austenitic structure at 70% Fe, according to the phase diagram for Fe-Ni at a comfortable temperature.

The intensities of the  $\gamma$ -Fe and the austenite are observed to have minimal influence on various process conditions shown in S2, S3, S7, and S9.

**3.3.1 Dislocation Density.** In wire arc additive manufacturing, the metal undergoes solidification at varying cooling rates. This process can lead to the generation of thermal stresses, which in turn, may result in dislocations within the deposited components. The dislocation density of a crystal may be calculated using x-ray diffraction (XRD) analysis. The process entails examining the widening of XRD peaks, which dislocations in the crystal lattice induce. Using Cu-K $\alpha$  radi-

ation, a  $2\theta$  range of  $20^\circ$  to  $120^\circ$  was scanned to get the x-ray diffraction patterns of selected samples which show maximum strength and minimum strength. The background correction and  $K\alpha_2$  stripping were performed on every x-ray diffraction profile for the line profile analysis. Then, taking into account the uniform deformation model (UDM), the average crystallite size, dislocation density, and microstrain were determined using the Williamson–Hall equation (Ref 20). The strain was considered to be constant across all crystallographic directions.

The Williamson–Hall equation is given by,

$$\beta \cos \theta = \frac{K\lambda}{D} + 4\epsilon \sin \theta \quad (\text{Eq 1})$$

$\beta$  is the full width at half maximum (FWHM) of the peak.  $K$  is the Scherrer constant (typically around 0.9).  $\lambda$  is the wavelength of the x-ray used (0.154 nm).  $D$  is the crystallite size.  $\theta$  is the Bragg angle.  $\epsilon$  Micro-strain

The intercept and slope from the plot (Fig. 10) of  $\beta \cos \theta$  versus  $4\sin \theta$  are used to get the values of  $D$  and  $\epsilon$ , respectively. The following formula was then used to determine the dislocation density of the specimens,

$$\rho = \frac{2\sqrt{3}(\epsilon)}{|b|D} \quad (\text{Eq 2})$$

where  $|b|$  is the Burgers vector (set to 0.287 nm for FCC structure), the deformation in a crystal lattice caused by dislocation is represented by the Burgers vector  $|b|$ . It is referred to as the most advantageous slip plane (closely packed plane)'s shortest lattice translation vector along the slip direction.

Figure 10 shows graphs for  $\beta \cos \theta$  versus  $4\sin \theta$  for different conditions, planes (h k l) for the different peaks are represented in the graphs. From the results of Table 5, it can be concluded that sample condition S3 at the bottom region has the maximum dislocation density as compared to the other samples. A material's strength and hardness improve with more dislocation density. This is because dislocations prevent additional dislocations from moving. Dislocations interact with one another when stress is applied, restricting their motion and making it

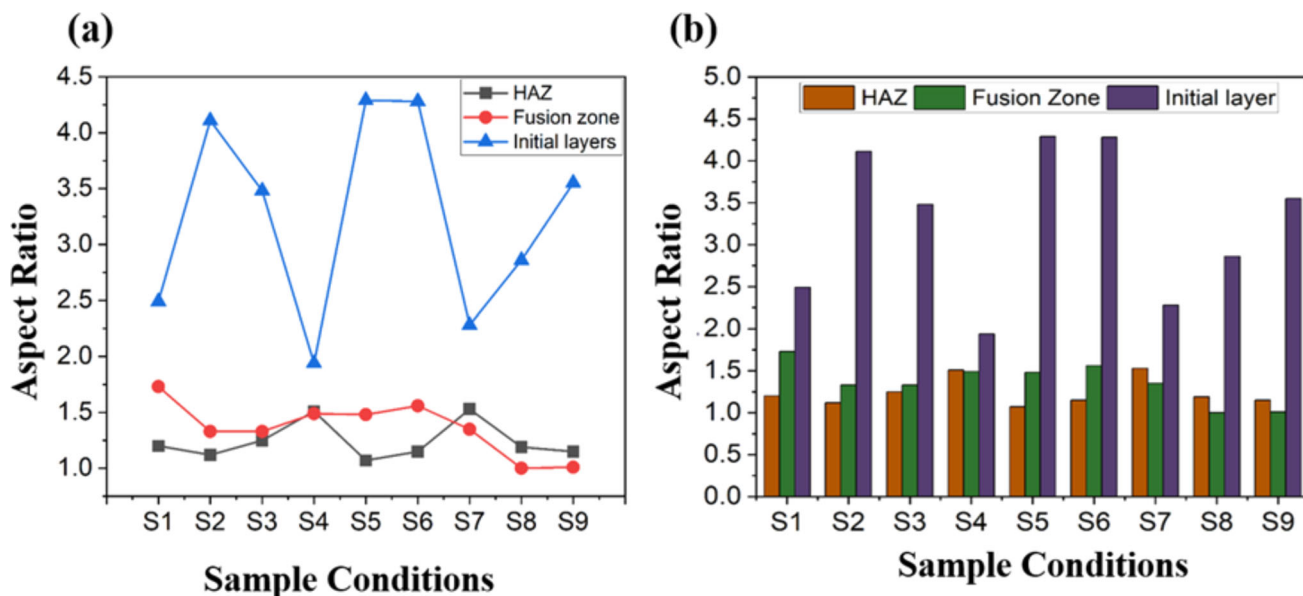


**Fig. 8** (a) Pattern for aspect ratio (b) aspect ratio comparison for different samples at junction region for heat-affected zone (HAZ), fusion zone, and initial layer

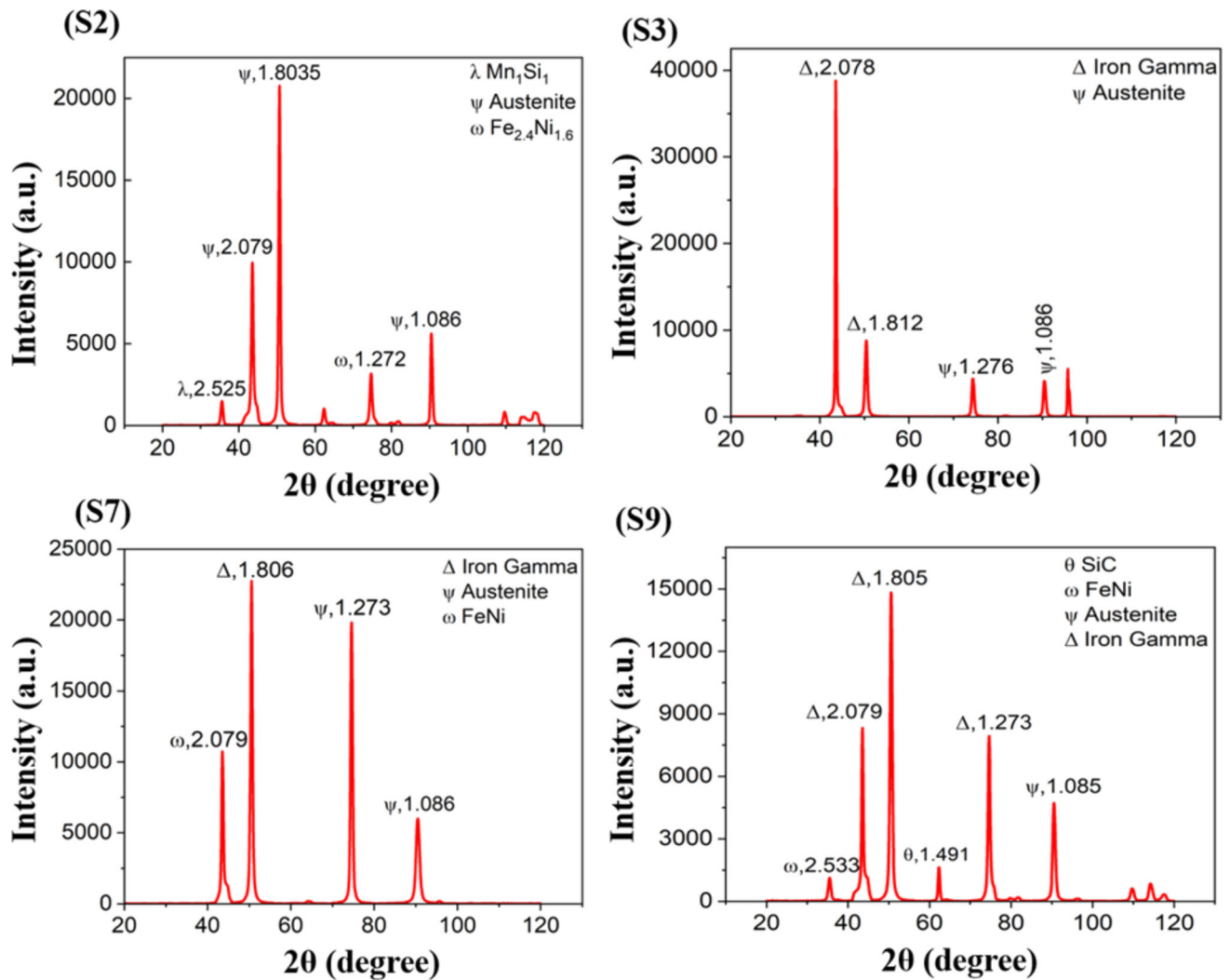


Fig. 9 XRD result for the as-deposited SS 316L alloy at the bottom region for different conditions S2, S3, S7, and S9

more difficult for the material to bend. From microhardness and tensile testing results also it can be justified that sample S3 at the bottom region has maximum hardness (201 HV) and maximum tensile strength (688 MPa) respectively among all samples. There is a relationship between a material's dislocation density and grain size. The number of grain boundaries that dislocations can interact with increases in materials with fine grain sizes. As a result, strength may be boosted by slowing down dislocation behavior. The microstructure at the bottom region of sample S3 is composed of equiaxed and dendritic grains.

Crystallite size and dislocation density often have an inverse relationship but one more parameter slope of  $\beta\cos\theta$  versus  $4S\sin\theta$  also plays an important role. Due to the presence of more grain boundaries in smaller crystallites, which can effectively act as barriers to dislocation motion. Smaller crystallite materials thus often have larger dislocation density. The relationship between dislocation density and crystallite size affects various material characteristics. For instance, a material may have great strength but low ductility if it has tiny crystallites and a high dislocation density.

#### 4. Tensile Properties

Tensile tests are conducted in the horizontal direction at the bottom zone of the as-deposited walls for all conditions. Elastic and plastic deformations are observed in all specimens before fracture. Notably, the samples exhibited tensile properties surpassing the standard values for wrought SS 316L, including ultimate tensile strength (UTS) of 582 MPa and yield strength (YS) of 280 MPa (Ref 12). Table 6 presents the ultimate tensile strength, yield strength, and elongation percentage for each sample, all demonstrating favorable properties compared to wrought SS 316L.

Stress-strain curves are plotted by keeping different travel speeds constant and by varying current values. Figure 11(a) plotted at a travel speed of 200 mm/min and current of 100 A, 120 A, and 140 A, similarly Fig. 11(b) at a travel speed of 240 mm/min and current of 100 A, 120 A, and 140 A, and Fig. 11(c) at travel speed 280 mm/min and current 100 A, 120 A, and 140 A.

Figure 12 shows a comparison of the tensile characteristics of the nine samples. The ultimate tensile strength and yield strength of WAAM-deposited SS 316L walls vary from 670 to 688 MPa and 316 to 360 MPa, respectively, in the depositing

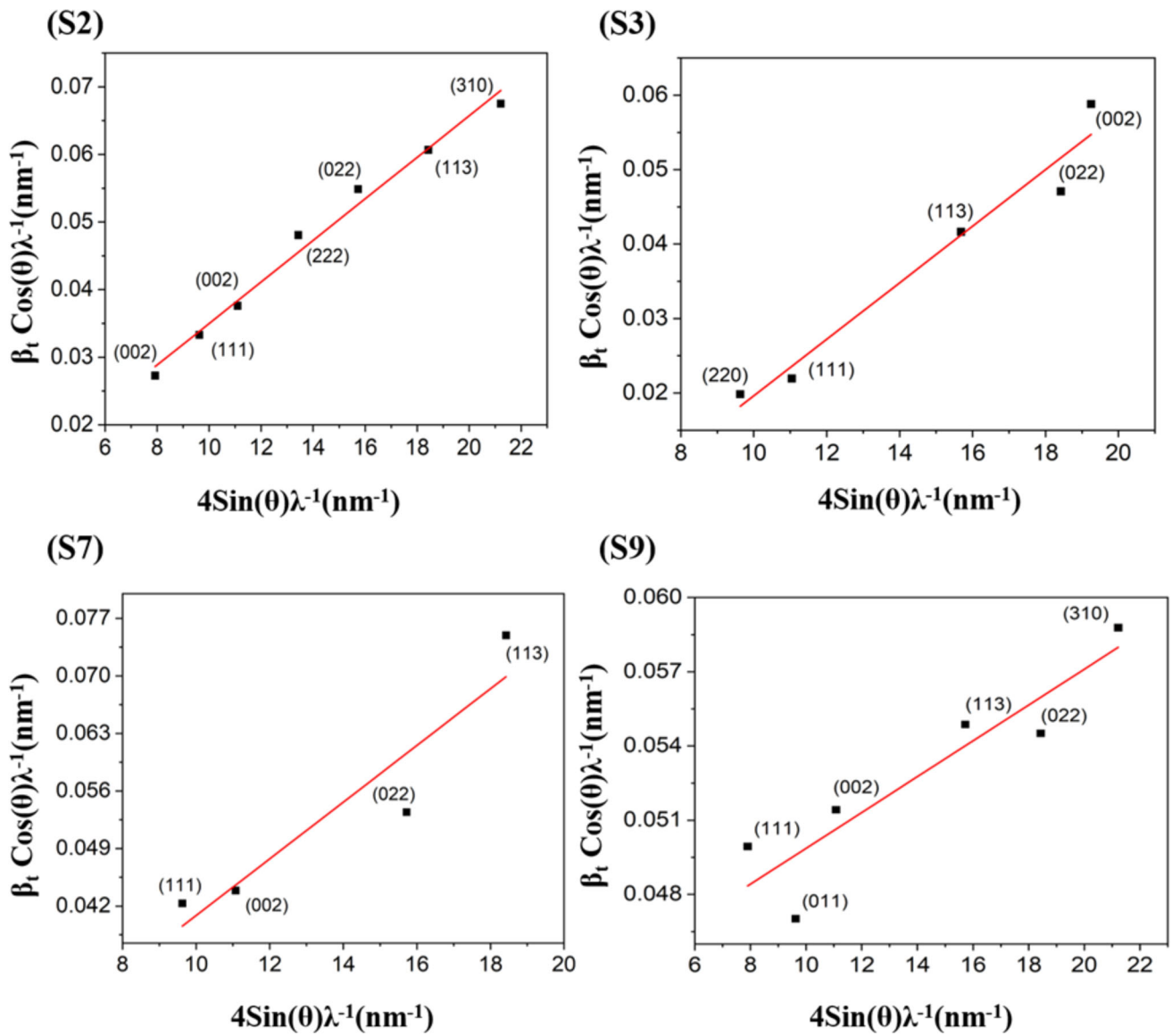


Fig. 10  $\beta_t \cos\theta$  versus  $4\sin\theta$  the Williamson–Hall (W–H) plots for different conditions

Table 5 Dislocation density for the WAAM-deposited samples

Samples	Crystallite size, D-nm	Dislocation density, $\text{nm}^{-2}$	Micro strain	Hardness, HV
S2 (Bottom)	212.26	$1.7457 \times 10^{-4}$	0.00307	190
S3 (Bottom)	44.019	$9.9220 \times 10^{-4}$	0.00381	201
S7 (Bottom)	21.11	$4.1109 \times 10^{-4}$	0.00243	170
S9 (Bottom)	140.84	$2.9362 \times 10^{-4}$	0.00345	179

direction. The horizontal specimens' elongation which ranges from 39.78 to 51.08% is equally variable. The inhomogeneity of microstructures due to different amounts of heat generation is what causes the difference in tensile properties (Ref 14).

Finer grains generated due to rapid cooling contribute to higher tensile strength, as described by the Hall–Petch equation (Ref 18), which states that material strength is inversely proportional to the square root of the average grain diameter. As grain size decreases, the material's density of grain boundaries

increases, impeding dislocation motion during deformation and resulting in increased strength (Ref 21). Fluctuations in strength in WAAM of SS 316L are caused by the complex cyclic thermal history of the process. Specifically, in the bottom zone, continuous remelting of layers results in the formation of overlapping melt boundaries, leading to the presence of columnar and equiaxed dendrites. These dendritic structures contribute to variations in strength within the bottom zone of the fabricated components (Ref 22). The results indicate that

the ultimate tensile strength (UTS) ranges from 670 MPa to 688 MPa. The maximum tensile strength is 688 MPa, at a current value of 100 A, the highest travel speed of 280 mm/min, and a gas flow rate of 20 L/min is obtained. On the other

**Table 6** Values of ultimate tensile strength, yield strength, and % elongation

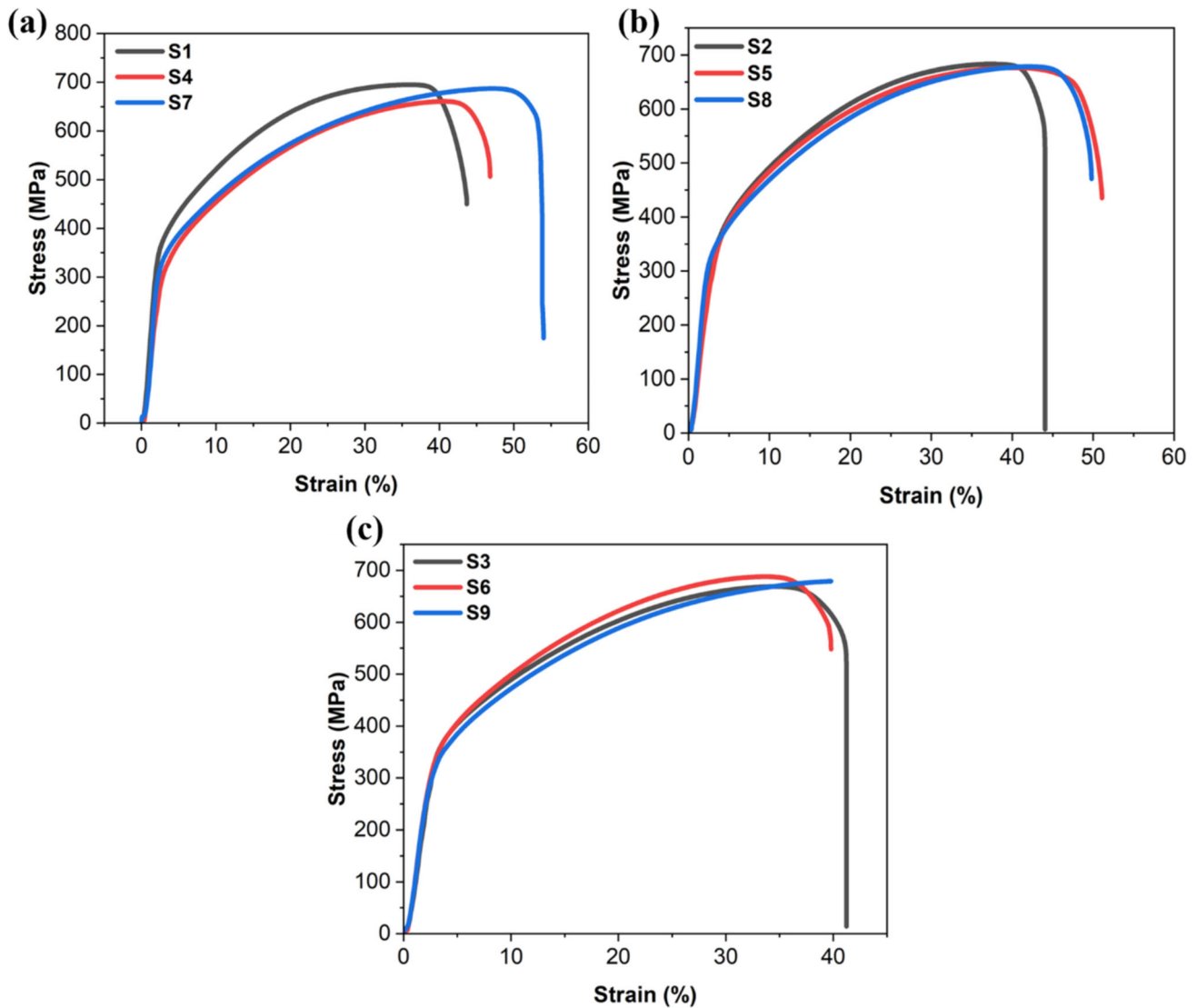
Experiment No.	YS, MPa	UTS, MPa	Elongation, %
S1	358	671	45.69
S2	348	683	44.04
S3	344	688	41.22
S4	316	675	46.81
S5	363	679	51.08
S6	360	687	39.78
S7	349	670	53.99
S8	322	673	49.79
S9	351	686	47.37

hand, the maximum elongation is observed at current 140 A, a travel speed of 200 mm/min, and a gas flow rate of 20 L/min, as per the specified conditions.

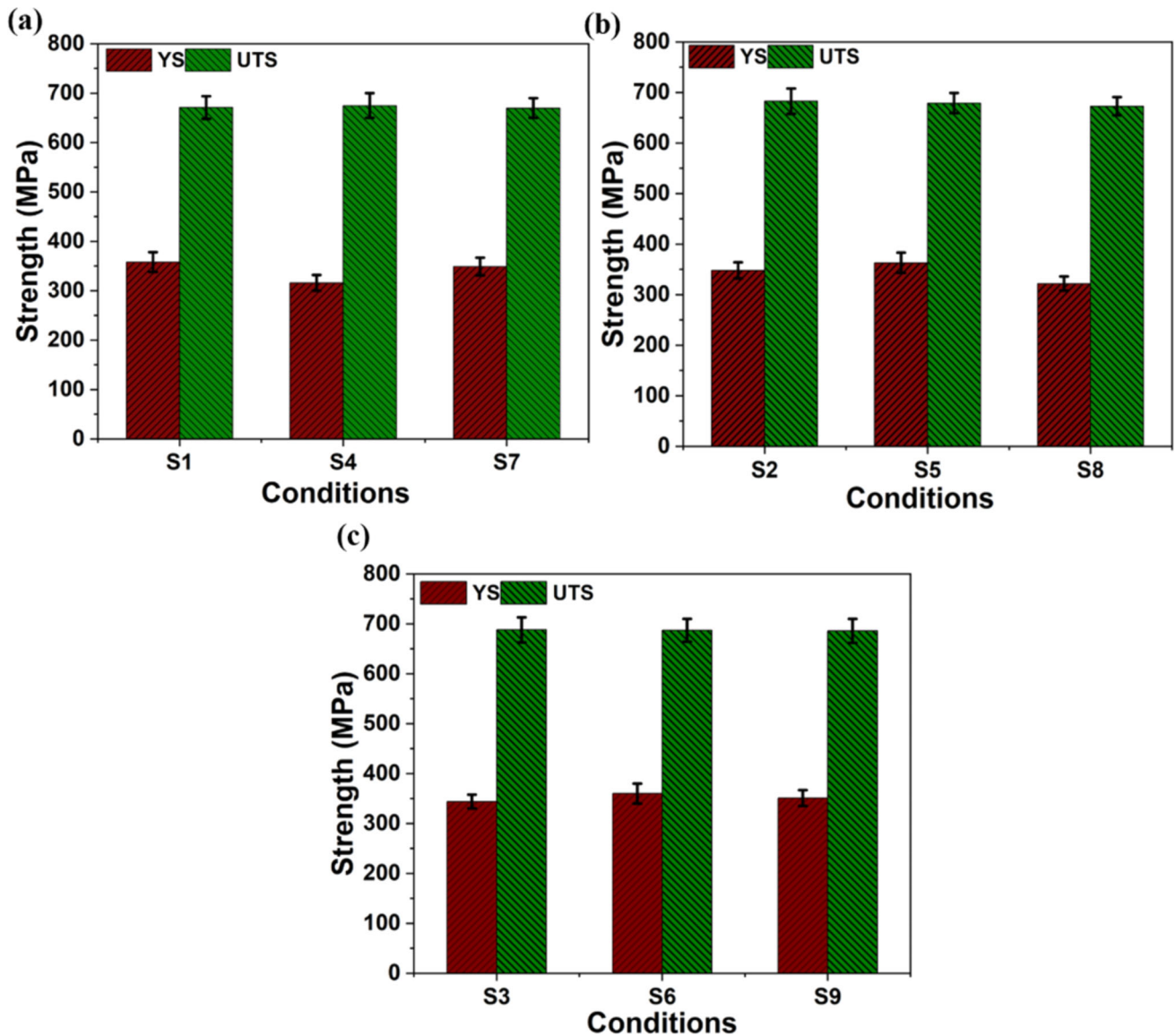
In this analysis, the tensile strength was selected as the output parameter to evaluate the strength of the as-deposited walls. A higher tensile strength indicates better quality. Therefore, the input parameters were optimized using the “larger the better” criteria.

Figure 13 and 14 show that with increasing the current the tensile strength is decreasing. Lower welding current reduces heat input, while increased gas flow helps in faster heat removal, resulting in finer microstructure and improved mechanical properties, including higher tensile strength. Similarly, with increasing the welding speed, the tensile strength is increasing due to shorter heating duration and faster cooling. The darker region indicates higher tensile strength. It is evident that increasing the travel speed results in higher tensile strength. For larger the better condition, the optimum conditions are 100 A current, 280 m/min travel speed, and 15 L/min gas flow rate.

A 95% confidence level was utilized for the ANOVA test to determine the most significant variable. The findings indicate that travel speed has the highest influence, followed by current



**Fig. 11** Stress-strain curves at constant travel speed (a) 200 mm/min, (b) 120 mm/min, and (c) 140 mm/min and different current values 100 A, 120 A, and 140 A



**Fig. 12** Ultimate tensile strength and yield strength at constant travel speed (a) 200 mm/min, (b) 240 mm/min, and (c) 280 mm/min and different current values 100 A, 120 A, and 140 A

and gas flow rates. The achieved R-squared values are 90.03% and 84.05% (adj.), respectively. R-Sq. and R-Sq. (adj.) are also called determination coefficient which shows the goodness of fit. Among the variables, only travel speed has a *P*-value less than 0.05, suggesting a reasonable likelihood of impacting the tensile strength of the wall.

The ANOVA analysis demonstrated that travel speed was the most influential input factor, followed by current and gas flow rate. Travel speed had the highest contribution of 84.05%, while current contributed 4.60% and gas flow rate contributed 1.37% to the overall variation in the tensile strength shown in Table 7.

## 5. Microhardness Analysis

The standard hardness value specified for wrought SS 316L is 172 HV (Ref 22). It is noteworthy that the hardness values obtained from the nine experiments are close to the standard

value. Table 8 presents the hardness values for the top, middle, and bottom zones in different experimental conditions from the results it can be noticed that hardness varies from 170 to 201 HV (Table 9).

The maximum observed value is 201 HV at 100 A current, 280 mm/min travel speed, and 20 L/min gas flow rate. This is because a higher gas flow rate promotes faster cooling, resulting in finer grain structure and improved metallurgical bonding, lower current leads to lower heat accumulation, promoting the formation of finer grains, and reducing the likelihood of grain coarsening (Ref 12). Higher travel speed allows for more rapid cooling and solidification, promoting the formation of a refined microstructure with a smaller grain size, which contributes to increased hardness (Ref 13).

The presence of finer grains in the material enhances its hardness. In a coarse-grained microstructure, where grains are larger, there are fewer grain boundaries compared to a fine-grained microstructure with smaller grains (Ref 14). Grain boundaries act as obstacles to dislocation movement, which are

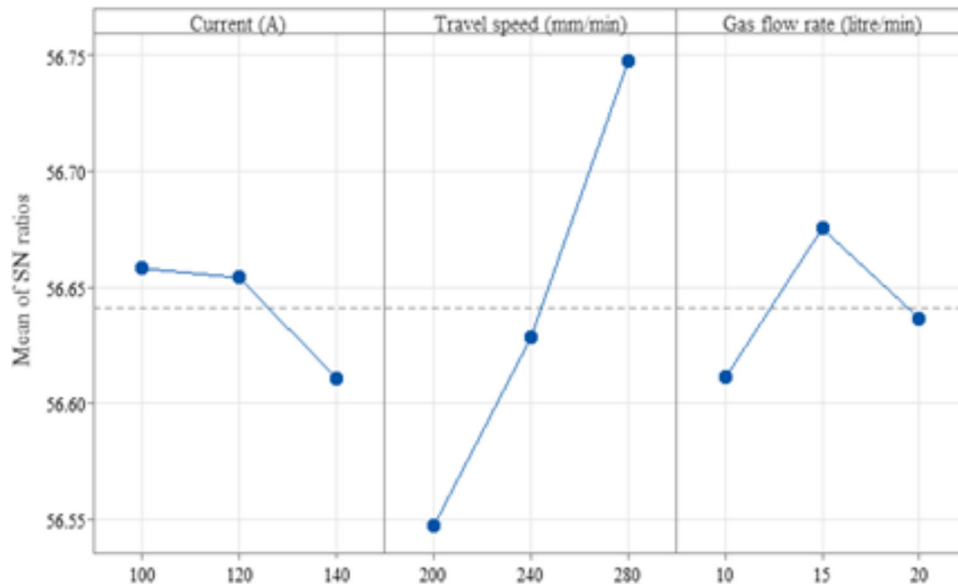


**Fig. 13** Main effect plot for SN ratio (tensile strength)

defects allowing plastic deformation. Dislocations can freely move within grains in a coarse-grained structure, enabling easier plastic deformation and resulting in lower hardness (Ref 15). Conversely, in a fine-grained structure, dislocations encounter grain boundaries more frequently, impeding their movement and increasing resistance to plastic deformation (Ref 21). This increased resistance leads to higher hardness as the material becomes harder to deform.

Taguchi analysis was employed to determine the optimal parameters for achieving maximum hardness. The objective was to obtain the highest possible hardness value. Therefore, the input parameters were evaluated based on the “larger the better” criteria. The main effect plot indicates that hardness increases as current decreases and travel speed increases Fig. 15 and 16.

Increasing the travel speed during WAAM of SS 316L can result in higher hardness due to shorter heating duration and faster cooling. Reducing the welding current reduces heat input, while increasing gas flow facilitates faster heat removal, leading to a finer microstructure and improved mechanical properties, including higher hardness.

In Fig. 17(a), the darker green region indicates higher hardness. It is evident that higher hardness is achieved when the travel speed is increased, and the current is kept relatively lower. Therefore, the optimal combination for achieving higher hardness in the WAAM process involves using a higher travel speed and lower current values. Similarly, different parameter combinations from the contour plots yield optimum hardness values.

Figure 17 presents contour plots that analyze the impact of input parameters, namely gas flow rate, travel speed, and current, on the hardness of SS 316L deposits produced through WAAM. These plots offer valuable insights into the relationship between these parameters and the mechanical properties of the material. By examining these plots, manufacturers and researchers can identify the optimal parameter combinations to achieve the desired hardness. This knowledge is crucial for process optimization, quality control, and meeting the dimensional requirements of manufactured components.

ANOVA analysis revealed that the most significant input factors were current, followed by travel speed and gas flow rate. The achieved values for R-Sq. and R-Sq. (adj.) are 94.28% and 90.85%, respectively. Only current and travel speeds exhibit a *P*-value of less than 0.05, indicating a reasonable chance that they may impact the hardness of the wall.

The current demonstrated the highest contribution of 72.08%, while travel speed contributed 18.02%, and gas flow rate contributed 4.18% toward the observed variations in the results.

Although the optimization of process conditions for maximization of tensile strength and hardness is performed using the Taguchi L9 orthogonal array, it is uncertain to predict the material behavior at various strains, and temperatures in the actual conditions. Therefore, in Sect. 6, the authors further estimated the parameters for the Johnson–Cook plasticity model for the various process conditions.

## 6. Johnson–Cook (J–C) Model

Johnson Cook (J–C) model is used to estimate an empirical relation for the SS 316L and to understand its behavior in various strains and temperatures. According to the J–C model, the flow stress is expressed as Eq 3 (Ref 17).

$$\sigma = (A + B\varepsilon^n)(1 + C \ln \varepsilon^*)(1 - T^{*M}) \quad (\text{Eq 3})$$

where *A* is the yield stress at reference temperature and strain rate, *n* is the exponent of strain hardening, *B* is the strain hardening coefficient,  $\varepsilon$  is the true strain,  $\varepsilon^* = \varepsilon/\varepsilon_{\text{ref}}$  is the dimensionless strain rate with being the strain rate ( $\text{s}^{-1}$ ), ref. the reference strain rate ( $\text{s}^{-1}$ ), and *T\** is homologous temperature, the equation is as follows:

$$T^* = \frac{T - T_{\text{ref.}}}{T_m - T_{\text{ref.}}}$$

where *T<sub>m</sub>* is the material’s melting point, *T* is the temperature at which it would deform, and *T<sub>ref</sub>* is the reference temperature

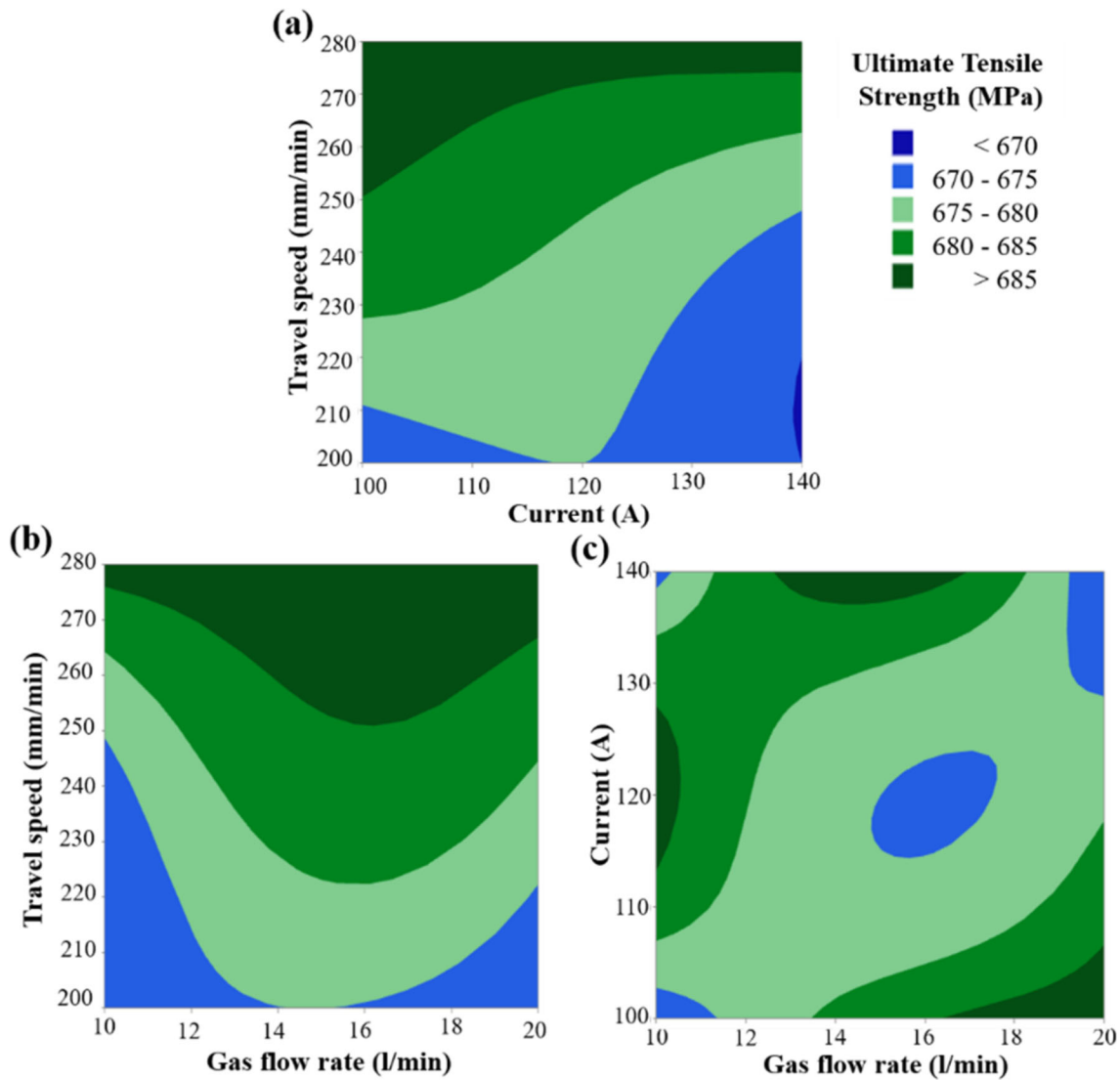


**Fig. 14** Contour plot concerning tensile strength versus (a) travel speed and current, (b) gas flow rate and current, and (c) gas flow rate and travel speed

**Table 7** Analysis of variance (tensile strength)

Source	DF	F Value	P Value	% Contribution
Current, A	1	2.31	0.189	4.60
Travel speed, mm/min	1	42.16	0.001	84.05
Gas flow rate, L/min	1	0.69	0.445	1.37
Error	5			10
Total	8			
R-Sq.				90.03%
R-Sq. (adj.)				84.05%

( $T \geq T_{ref}$ ). The material constants  $C$  and  $m$  stands for the thermal softening exponent and the coefficient of strain rate hardening, respectively. Thus, the strain hardening effect, strain rate strengthening effect, and temperature impact are represented by the three items in the formula from left to right, with the overall effect being derived by multiplying the aforementioned elements. Figure 18 shows the process for calculating the material constant.

**Table 8** Microhardness (HV) values for all conditions at different locations

Exp. No.	Top (HV)	Middle (HV)	Bottom (HV)
S1	183	184	186
S2	192	182	190
S3	179	188	201
S4	175	178	178
S5	173	177	183
S6	190	182	181
S7	175	177	170
S8	178	173	174
S9	181	172	179

In the current study, the reference temperature is set to  $T_{ref} = 100$  K, and the reference strain rate  $\dot{\epsilon}_{ref} = 1$  s<sup>-1</sup>. Due to the variation of process parameters, the yield stress varies from  $A = 316$  to  $363$  MPa. The melting point ( $T_m$ ) of SS 316L is  $1673$  K.

**Table 9 Analysis of variance (hardness)**

Source	DF	F Value	P Value	% Contribution
Current, A	1	63.03	0.001	72.08
Travel speed, mm/min	1	15.76	0.011	18.02
Gas flow rate, L/min	1	3.65	0.114	4.18
Error	5			6
Total	8			
R-Sq.				94.28%
R-Sq. (adj.)				90.85%

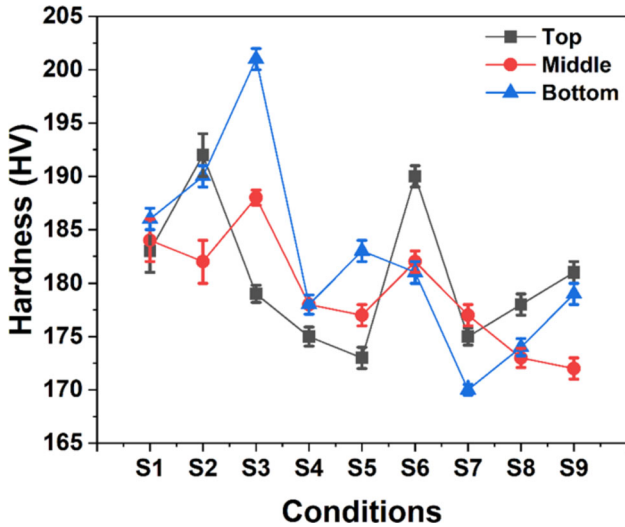


**Fig. 15** Variation of average hardness for different samples at different locations

**6.1 Procedure of the J-C Model**

Three steps can be used to compute the constants of the J-C equation: first, ignore strain rate hardening and thermal softening; second, observe the effects of strain rate hardening; and third, ignore thermal softening. The third stage focuses on the impact of thermal softening while ignoring strain rate hardening.

- *Step 1:* When reference strain rate and temperature are used, Equation (3) of flow stress will decrease to  $\sigma = (A + B\epsilon^n)$  as shown in Fig. 18. Strain rate hardening and heat softening may be ignored in this stage.
- *Step 2:* With a set plastic strain at reference temperature: It is possible to see the strain rate hardening impact, and the thermal softening effect will be ignored. Flow stress Eq 3 becomes  $\sigma = (A + B\epsilon^n) (1 + C \ln \epsilon^*)$ .
- *Step 3:* With a set plastic strain and a reference strain rate: Eq 3 simplifies to equation  $\sigma = (A + B\epsilon^n) (1 - T^{*m})$  in this stage, where the impact of thermal softening will be noticed and strain rate hardening will be disregarded (Fig. 19).

The J-C model, which was addressed above, relates with  $\sigma$  to temperature, and strain rate. The model contains just a few constants,  $A$ ,  $B$ ,  $n$ ,  $C$ , and  $m$ , whose values for different conditions have been approximated. The information is provided in Table 10. By determining the intercept and slope of  $\ln(\sigma - A)$  versus  $\ln \epsilon$ , as illustrated in Fig. 20, the constants  $B$  and  $n$  are determined from step 1 (Fig. 18) at the reference temperature and strain rate.

The slopes of  $\sigma/(A + B\epsilon^n)$  versus  $\ln \epsilon^*$  and  $\ln(1 - \sigma/(A + B\epsilon^n))$  versus  $\ln T^*$ , which are shown in Fig. 18 step 2 and step 3 respectively, are used to determine the values of  $C$

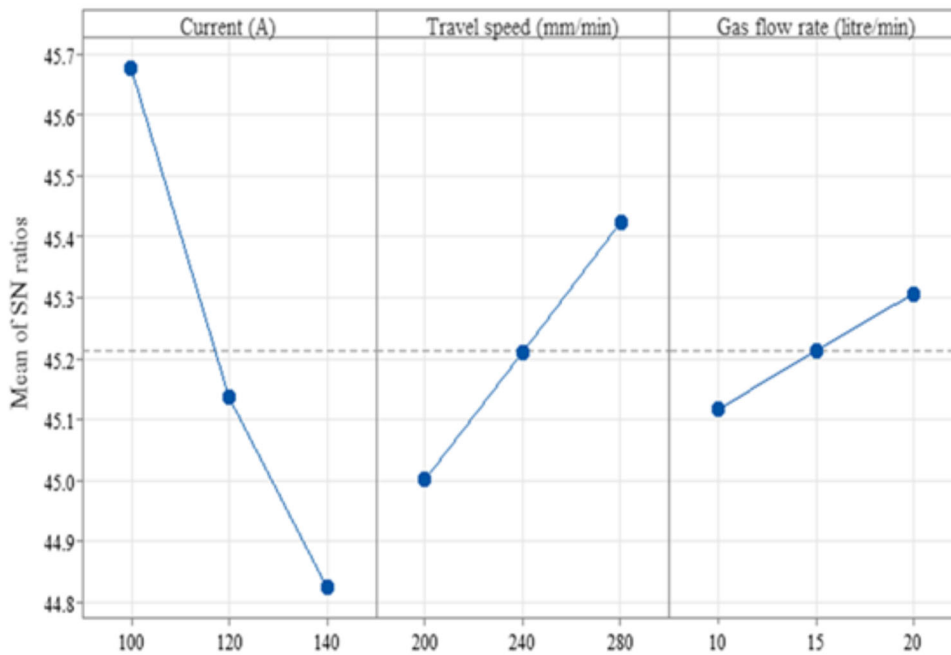


**Fig. 16** Main effect plot for SN ratio (hardness)



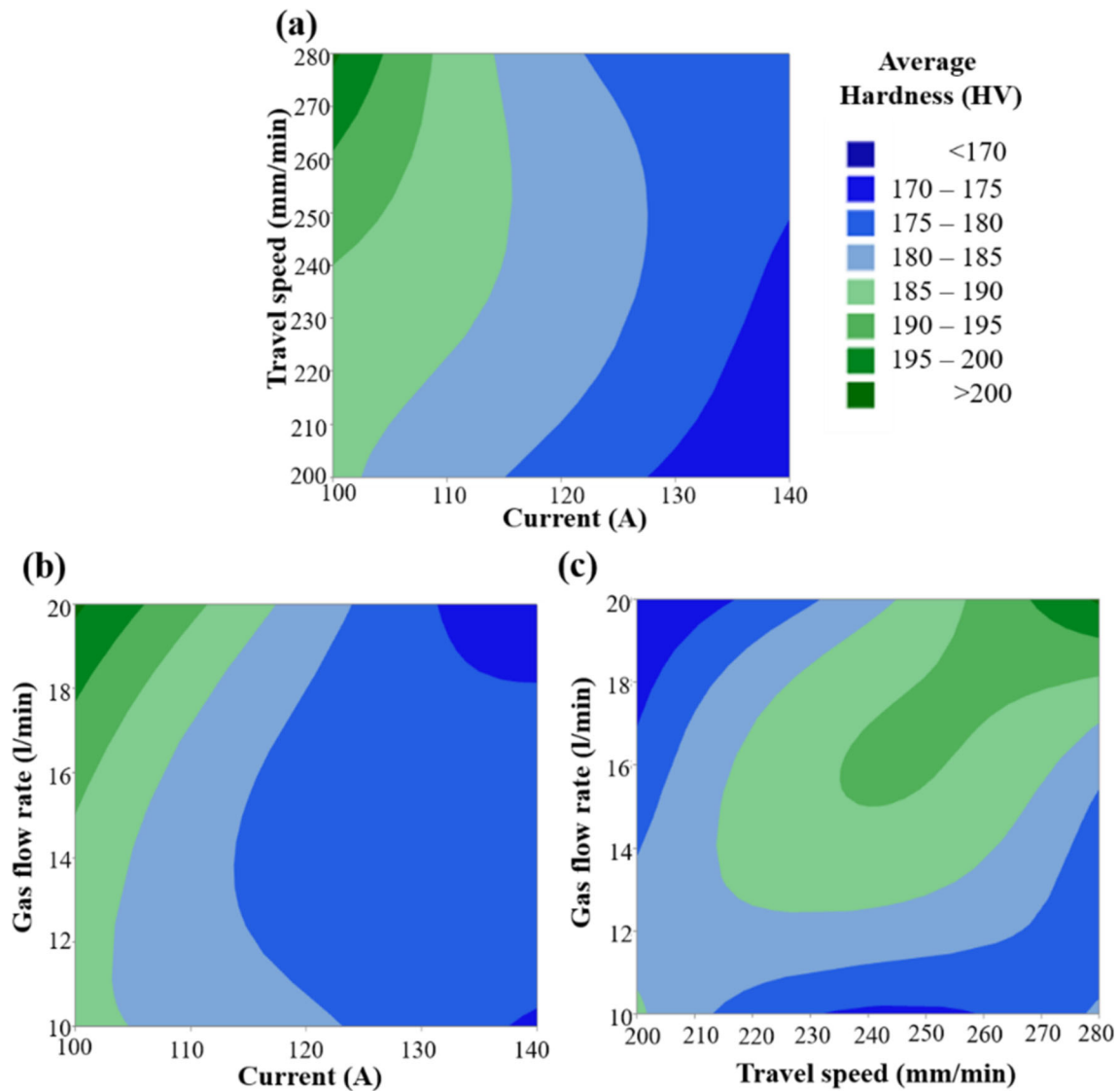


**Fig. 17** Contour plot concerning hardness versus (a) travel speed and current, (b) gas flow rate and current, and (c) gas flow rate and travel speed

and  $m$ . The final equation may be stated as Eq (S1) to Eq (S9) by replacing all the aforementioned values of the material constant as indicated in Table 10. The graph is plotted in between  $\sigma/(A + B\epsilon^n)$  versus  $\ln \epsilon^*$  for the value of constant  $C$  and the value of  $\epsilon^*$  is evaluated by taking the ratio of  $\epsilon/\epsilon_{ref}$ . Constant  $m$  is evaluated by taking the slope of graph  $\ln(1 - \sigma/(A + B\epsilon^n))$  versus  $\ln T^*$ , where  $T^*$  is defined as the ratio of  $T - T_{ref}/T_m - T_{ref}$ . After regression, the material constants of the JC model for SS 316L are given in Table 10.

A material's strain hardening constant, commonly referred to as the strain hardening exponent or work-hardening exponent, is a characteristic that describes how a material's strength grows with plastic deformation. The rate at which material gets strength when it experiences plastic deformation, in Eq 3 hardening exponent represented by ' $n$ ' (Ref 19).

A material with a higher ' $n$ ' value exhibits strong strain hardening, which causes a fast increase in strength with deformation. The higher dislocation density in materials usually results in more strain hardening. In Sect. 3.3.1 dislocation density is explained in detail where it can be observed that

sample condition S3 has maximum dislocation density which can be compared with strain hardening exponent ( $n$ ) Table 10 where sample S3 has the highest value (0.12974) of the hardening exponent. This is because a larger dislocation density creates more barriers in the way of additional dislocations moving, which makes it more challenging for the material to deform plastically. As a result, with plastic deformation, the material's strength grows more quickly.

In conclusion, a material often experiences a greater rise in strength with plastic deformation if its dislocation density is larger. This is because a higher dislocation density typically results in a higher strain hardening exponent. In materials engineering, this connection is crucial for adjusting material characteristics to fulfill certain performance demands (Ref 20).

The J-C equation for all the conditions: The following equation can be generated by keeping constant values in Eq 3 for different conditions.

$$\sigma = (358 + 2.330\epsilon^{0.119})(1 + 3.046 \ln \epsilon^*)(1 - T^{*2.263}) \quad (S1)$$

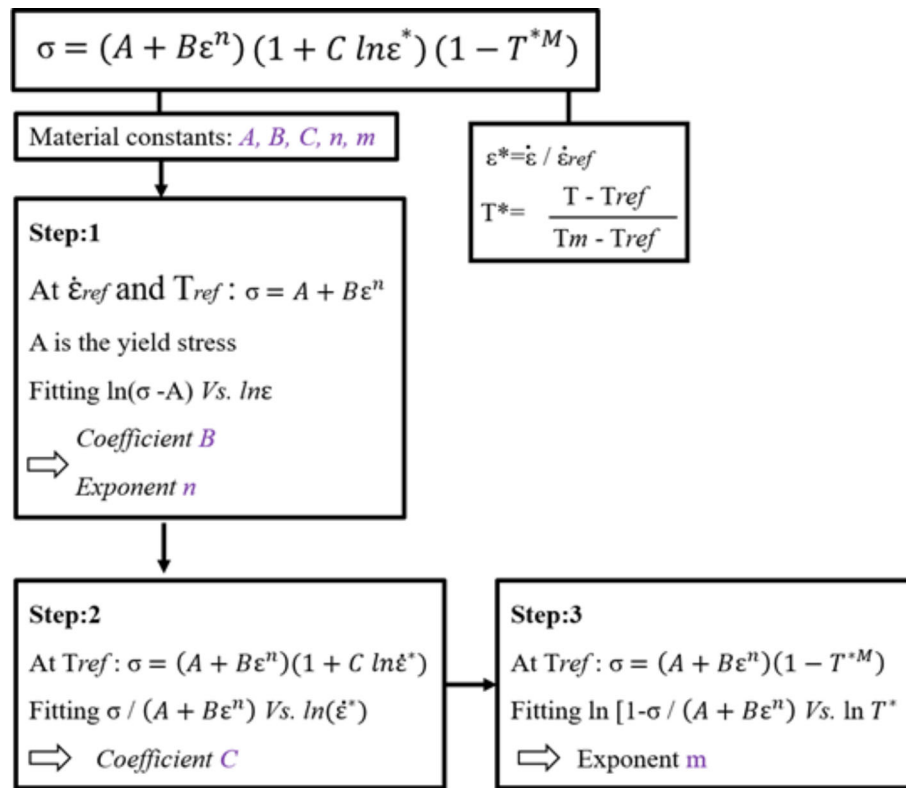


Fig. 18 The procedure of Johnson–Cook model

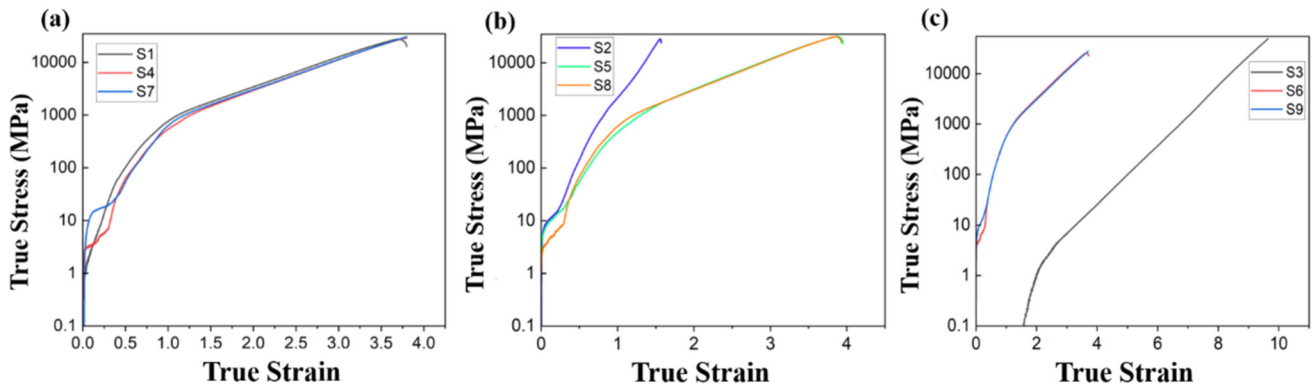


Fig. 19 True stress–strain results of different samples at different deposition conditions

Table 10 Parameters for the J–C model for different conditions

Constants	A	B	C	n	m
S1	358	2.330	3.046	0.11955	2.26339
S2	348	2.3150	3.046	0.12174	2.26339
S3	344	2.32079	3.046	0.12974	2.26339
S4	316	2.3038	3.046	0.127377	2.26339
S5	363	2.3075	3.046	0.12646	2.26339
S6	360	2.3196	3.046	0.12289	2.26339
S7	349	2.3257	3.046	0.12113	2.26339
S8	322	2.31400	3.046	0.125	2.26339
S9	351	2.3144	3.046	0.12454	2.26339

$$\sigma = (348 + 2.315\varepsilon^{0.121}) (1 + 3.046 \ln \varepsilon^*) (1 - T^{*2.263}) \quad (S2)$$

$$\sigma = (344 + 2.330\varepsilon^{0.129}) (1 + 3.046 \ln \varepsilon^*) (1 - T^{*2.263}) \quad (S3)$$

$$\sigma = (351 + 2.330\varepsilon^{0.124}) (1 + 3.046 \ln \varepsilon^*) (1 - T^{*2.263}) \quad (S9)$$

## 7. SEM Analysis on Fracture Surface

The broken surfaces of the horizontal tensile samples from the bottom for condition S3 are depicted in Fig. 21 using Scanning electron microscope (SEM) images. Images at higher magnification of the dimpled regions also showed the presence

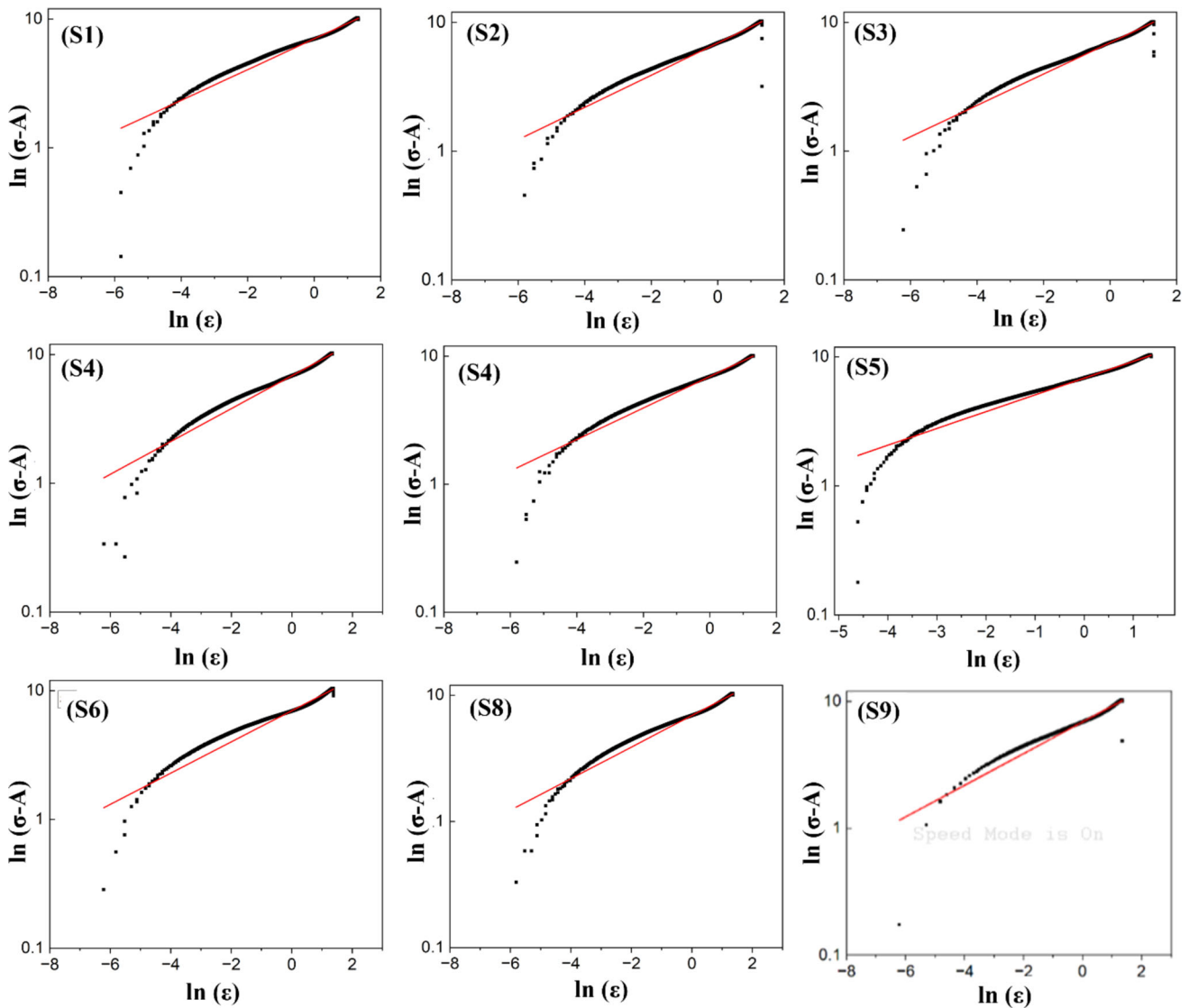


**Fig. 20** Graph between strain and  $(\sigma-A)$  in logarithmic scale for different samples

of inclusion particles in the dimples' centers. The fractographs revealed the existence of voids, dimples, honeycomb structure, riverine structure, and cleavage facets and dimples seen by the arrows in the lower magnification photos, demonstrating a mixed-mode brittle and ductile fracture. These inclusions' absence of Fe and predominant Mn, Si, and O compositions point to their MnO, SiO<sub>2</sub> nature (Ref 18). It is established that there are micro gaps at the fracture surface of the tensile sample as-deposited sample compared to the industrial grade, and these microvoids help to boost the load-bearing capacity of the WAAM sample. As a result, the WAAM sample's ultimate strength is greater than the industrial grade. The as-deposited samples for the best condition concerning the mechanical property show dimples, and river facets as shown in Fig. 21.

Similar fracture modes from ductile to mixed and brittle modes for the bottom region, respectively, of a WAAM fabricated 2Cr13 component have also been seen in earlier research (Ref 18). Inclusions may cause voids to emerge, which may impede a material's ability to fracture. An increase in inclusions may encourage the formation of voids, which may

reduce the active load area of the specimen under tension and eventually cause a premature fracture. On the other hand, a large number of microvoid nucleation sites can postpone fracture and increase the ductility of the material (Ref 18).

## 8. Conclusions

The present work on wire arc additive manufacturing of SS 316L has drawn the following conclusions:

- The SS 316L walls were successfully constructed without any significant flaws. The columnar austenite dendrites and  $\delta$ -ferrite found inside the austenitic matrix make up the characteristic microstructure of SS 316L walls. Columnar dendrites epitaxially develop from the remelted zone of the preceding layer in a particular deposited layer in the build direction, and at the layer's top, they change into coarse columnar structures with equiaxed grains.

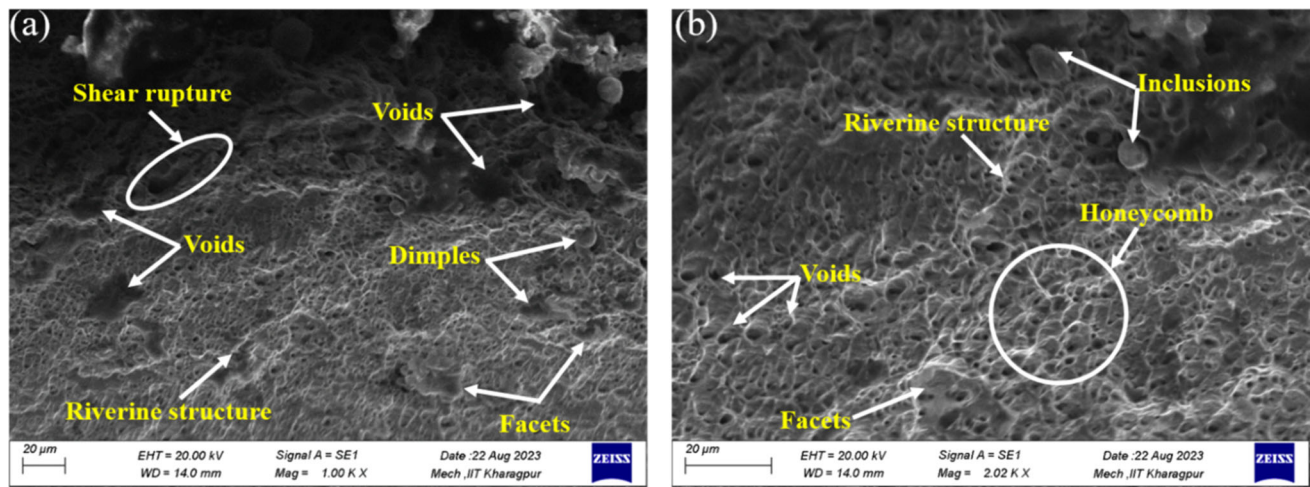


**Fig. 21** SEM fractographs of the tensile specimen extracted from bottom region specimens-S3

- The maximum and minimum grain size at the fusion region are  $19\ \mu\text{m}$  and  $8\ \mu\text{m}$  respectively for as-deposited samples manufactured with process conditions of 120 A—200 mm/min-15 L/min (current–travel speed –gas flowrate) and 120 A—280 mm/min—10 L/min, respectively.
- Optimized conditions for tensile properties are 100 A current, 280 mm/min travel speed, and 20 L/min gas flow rate with a UTS value of 688 MPa in the depositing direction. The travel speed significantly impacts tensile strength among all the input parameters, followed by current and gas flow rate. Current holds the highest influence, followed by travel speed and gas flow rate in terms of max hardness (201HV) with optimum conditions of 100 A current, 280 mm/min travel speed, and 20 L/min gas flow rate.
- An empirical relation to understanding the behavior of the material at various strains and temperatures is established  $\sigma = (351 + 2.330 \varepsilon^{0.124}) (1 + 3.046 \ln \varepsilon^*) (1 - T^{*2.263})$ .
- The major phases are observed to be austenite, Fe-Ni, and  $\gamma$ -Fe in condition S2 highest peak occurred at angle  $50^\circ$  with the composition of iron-nickel and iron silicide carbide with d-spacing 2.07923 and 0.94355, respectively. The dislocation density is observed to be varied from  $1.745 \times 10^{-4}$  to  $9.922 \times 10^{-4}\ \text{nm}^{-2}$  and the microstrain is varied from  $2.43 \times 10^{-3}$  to  $3.8 \times 10^{-3}$ .
- The as-deposited samples for the best condition concerning the mechanical property show dimples, and river facets.

### Acknowledgment

The authors would like to thank the metallurgy laboratory of the Department of Mechanical Engineering, Sardar Vallabhbhai National Institute of Technology Surat. Thanks to Dr. Vishvesh Badheka from the Department of Mechanical Engineering, School of Technology, Pandit Deendayal Energy University, Raisan, Gandhinagar, for providing us with facilities.

### References

1. E. Taban and O.O. Oladimeji, Microstructure, Mechanical and Corrosion Behavior of Additively Manufactured Steel: A Review (Part 1), *Mater. Test.*, 2020, **62**(5), p 503–516
2. R. Li, G. Wang, X. Zhao, F. Dai, C. Huang, M. Zhang, X. Chen, H. Song, and H. Zhang, Effect of Path Strategy on Residual Stress and Distortion in Laser and Cold Metal Transfer Hybrid Additive Manufacturing, *Addit. Manuf. Manuf.*, 2021, **1**(46), 102203
3. S.W. Williams, F. Martina, A.C. Addison, J. Ding, G. Pardal, and P. Colegrove, Wire+ Arc Additive Manufacturing, *Mater. Sci. Technol.*, 2016, **32**(7), p 641–647
4. J. Zhang, X. Wang, S. Paddea, and X. Zhang, Fatigue Crack Propagation Behavior in Wire+ Arc Additive Manufactured Ti-6Al-4V: Effects of Microstructure and Residual Stress, *Mater. Des.*, 2016, **15**(90), p 551–561
5. T.S. Senthil, S.R. Babu, M. Puviyarasan, and V. Dhinakaran, Mechanical and Microstructural Characterization of Functionally Graded Inconel 825-SS316L Fabricated Using Wire Arc Additive Manufacturing, *J. Mark. Res.*, 2021, **1**(15), p 661–669
6. G.I. Khidhir and S.A. Baban, Efficiency of Dissimilar Friction Welded 1045 Medium Carbon Steel and 316L Austenitic Stainless Steel Joints, *J. Mark. Res.*, 2019, **8**(2), p 1926–1932
7. A. Saboori, A. Aversa, G. Marchese, S. Biamino, M. Lombardi, and P. Fino, Microstructure and Mechanical Properties of AISI 316L Produced by Directed Energy Deposition-Based Additive Manufacturing: A Review, *Appl. Sci.*, 2020, **10**(9), p 3310
8. M. Liberini, A. Astarita, G. Campatelli, A. Scippa, F. Montevercchi, G. Venturini, M. Durante, L. Boccardo, F.M. Minutolo, and A. Squillace, Selection of Optimal Process Parameters for Wire Arc Additive Manufacturing, *Procedia Corp.*, 2017, **1**(62), p 470–474
9. D.S. Mai, T.K. Doan, and H. Paris, Wire and Arc Additive Manufacturing of 308L Stainless Steel Components: Optimization of Processing Parameters and Material Properties, *Eng. Sci. Technol. Int. J.*, 2021, **24**(4), p 1015–1026
10. V. Kumar, A. Mandal, A.K. Das, and S. Kumar, Parametric Study and Characterization of Wire Arc Additive Manufactured Steel Structures, *Int. J. Adv. Manuf. Technol.*, 2021, **115**(5–6), p 1723–1733
11. F. Youheng, W. Guilan, Z. Haiou, and L. Liye, Optimization of Surface Appearance for Wire and Arc Additive Manufacturing of Bainite Steel, *Int. J. Adv. Manuf. Technol.*, 2017, **91**, p 301–313
12. A. Kumar and K. Maji, Selection of Process Parameters for Near-Net Shape Deposition in Wire Arc Additive Manufacturing by Genetic Algorithm, *J. Mater. Eng. Perform.*, 2020, **29**, p 3334–3352
13. A. Waqas, X. Qin, J. Xiong, H. Wang, and C. Zheng, Optimization of Process Parameters to Improve the Effective Area of Deposition in GMAW-Based Additive Manufacturing and Its Mechanical and Microstructural Analysis, *Metals.*, 2019, **9**(7), p 775

14. K. Venkatarao, The Use of Teaching-Learning-Based Optimization Technique for Optimizing Weld Bead Geometry As Well As Power Consumption in Additive Manufacturing, *J. Clean. Prod.*, 2021, **10**(279), 123891
15. J. Xiong, Y. Li, R. Li, and Z. Yin, Influences of Process Parameters on Surface Roughness of Multi-Layer Single-Pass Thin-Walled Parts in GMAW-Based Additive Manufacturing, *J. Mater. Process. Technol.*, 2018, **1**(252), p 128–136
16. L. Yuan, D. Ding, Z. Pan, Z. Yu, B. Wu, S. van Duin, H. Li, and W. Li, Application of Multidirectional Robotic Wire Arc Additive Manufacturing Process for the Fabrication of Complex Metallic Parts, *IEEE Trans. Industr. Inf.Industr. Inf.*, 2019, **16**(1), p 454–464
17. G. R. Johnson, A Constitutive Model and Data for Metals Subject to Large Strains, High Strain Rate and High Temperatures. In *Proc. of 7th Int. Symp. on Ballistics, The Hague*. 1983
18. J. Lunde, M. Kazemipour, S. Salahi, and A. Nasiri, Wire Arc Additive Manufacturing of AISI 420 Martensitic Stainless Steel: On as-Printed Microstructure and Mechanical Properties, *J. Mater. Eng. Perform.*, 2021, **30**(12), p 9181–9191
19. C. Huang, P. Kyvelou, and L. Gardner, Stress-Strain Curves for Wire Arc Additively Manufactured Steels, *Eng. Struct.Struct.*, 2023, **279**, 115628
20. G. Asala, J. Andersson, and O.A. Ojo, Analysis and Constitutive Modeling of High Strain Rate Deformation Behaviour of Wire–Arc Additive-Manufactured ATI 718Plus Superalloy, *Int. J. Adv. Manuf. Technol.*, 2019, **103**, p 1419–1431
21. S. Hossein Nedjad, M. Yildiz, and A. Saboori, Solidification Behaviour of Austenitic Stainless Steels During Welding and Directed Energy Deposition, *Sci. Technol. Weld. Join.*, 2023, **28**(1), p 1–17
22. M. Dinovitzer, X. Chen, J. Laliberte, X. Huang, and H. Frei, Effect of Wire and Arc Additive Manufacturing (WAAM) Process Parameters on Bead Geometry and Microstructure, *Addit. Manuf. Manuf.*, 2019, **26**, p 138–146

**Publisher's Note** Springer Nature remains neutral with regard to jurisdictional claims in published maps and institutional affiliations.

Springer Nature or its licensor (e.g. a society or other partner) holds exclusive rights to this article under a publishing agreement with the author(s) or other rightsholder(s); author self-archiving of the accepted manuscript version of this article is solely governed by the terms of such publishing agreement and applicable law.